AIAA AVIATION Forum
August 2-6, 2021, VIRTUAL EVENT
AIAA AVIATION 2021 FORUM

10.2514/6.2021-3205

Evaluating the Performance and Acoustic Footprint of Aircraft for Regional and Urban Air Mobility

Matthew A. Clarke* and Juan J. Alonso †
Department of Aeronautics and Astronautics, Stanford University, Stanford CA, 94305

The synthesis of semi-empirical and physics-based models to estimate aerodynamic loads, propulsion network performance and radiated noise of short-range commuter aircraft is presented in this paper. These methods can be classified as medium-fidelity, whereby predictions require a fraction of the computing cost of more expensive approaches such as CFD while maintaining a degree of accuracy sufficient to facilitate design optimization. A robust weight build-up method based on certification standards, component geometry and design loads is used to ascertain realistic estimates of takeoff gross weight. These analytical tools are integrated into SUAVE, a system-level simulation test bench for assessing the performance of manned and unmanned aircraft. The sizing of powertrain components is also discussed to highlight best practices in the approach to bring non-conventional vehicle configurations from pen-and-paper to the preliminary design stage. As the first of a series of publications outlining a framework to perform multidisciplinary design optimization, the aircraft studied in this paper cover the major vehicular configurations intended for regional and urban air mobility. These aircraft were simulated through a baseline mission to comparatively assess performance and acoustic footprint measured from ground level. A synopsis of the impact of battery cell cathode chemistry, mission profile and passenger capacity is subsequently held.

Nomenclature

AoA	=	aircraft angle of attack
AR	=	aspect ratio
b	=	wing span
C	=	c-rate
C_L	=	coefficient of lift
C_D	=	coefficient of drag
C_p	=	power coefficient
C_t	=	thrust coefficient
dQ	=	torque distribution
dT	=	thrust distribution
DL	=	disc loading
D	=	rotor diameter
E	=	battery energy
G	=	motor gear ratio
i	=	unit imaginary ($\sqrt{-1}$)
I	=	current
I_o	=	no-load current
$J_{mb}(x)$	=	Bessel function of order mB and argument x
k_x	=	wave number
K_v	=	motor speed constant
LiB	=	lithium-ion battery cell
L/D	=	lift-to-drag ratio
n	=	rotation rate, (rev/sec)
m	=	harmonic number
M	=	freestream Mach number
M_s	=	blade section Mach number
M_t	=	tip Mach number
MCA	=	mid-chord alignment of rotor blade
n	=	quantity of component
nmi	=	nautical mile
P	=	power
P_0	=	reference sound pressure, 2×10^{-5} Pa
P_L	=	loading component of R.M.S sound pressure
P_T	=	thickness component of R.M.S sound pressure
P_V	=	broadband component of R.M.S sound pressure
Q	=	torque
r	=	non-dimensional radius
R	=	rotor radius
R_0	=	internal resistance
$R.M.S$	=	root mean square
RPM	=	revolutions per minute
S	=	observer distance from rotor hub
S_{ref}	=	wing reference area
SPL	=	sound pressure level
t	=	flight time
$\hat{t}$	=	normalized flight time, t/t_{EOF}

*Ph.D. Candidate, Department of Aeronautics and Astronautics, AIAA Student Member
†Professor, Department of Aeronautics and Astronautics, AIAA Fellow

T	=	thrust
$TOGW$	=	takeoff gross weight
x_{fp}	=	vehicle footprint
x, y, z	=	cartesian coordinates
V	=	voltage
α	=	rotor thrust angle
η	=	efficiency
Ω	=	angular velocity
ϕ	=	tangential angle
ϕ_s	=	phase lag due to sweep
ϕ_t	=	blade twist angle relative to propeller plane
Ψ_L	=	normalized loading source transformation
Ψ_V	=	normalized thickness source transformation
ρ	=	air density
θ	=	observer angle relative to flight direction
ζ	=	power throttle

Subscripts

bat	=	battery
EOF	=	end of flight
g	=	gearbox
m	=	motor
max	=	maximum
OC	=	open-circuit
p	=	parallel arrangement of LiB in battery pack
$prop$	=	propeller
rot	=	rotor
s	=	series arrangement of LiB in battery pack
tot	=	total
UL	=	under-load

I. Introduction

The steady rise in urban populations in megacities around the world has placed the ability of their respective transportation networks to facilitate the increased demand under the spotlight [1]. Elaborate road networks, bridges and tunnels are all becoming more expensive to construct and difficult and maintain [2]. Despite federal and state initiatives to reduce the strain on highways and interstates, noise and air pollution continue to rise. Electrified ground transportation in the form of electric vehicles (EVs) has gone some way in reducing greenhouse gas emissions such as CO2 and NOx. However, there are rising concerns that future autonomous EVs will further increase congestion and strain current infrastructure as noted by Millard-Ball [3]. The concept of urban air mobility was hence birthed from this need to address growing demands for a faster, safer and more cost-effective solutions. This encapsulates the use of electric aircraft, both conventional fixed-wing and rotary-wing, as well as new electric short/vertical takeoff and landing aircraft (eS/VTOL) to facilitate transit.

Today, over 175 eS/VTOL concepts have been made public, varying both in the degree of disclosure and development [4]. With no established framework for developing new aircraft, conflicting ideas and predictions of performance have heretofore produced no consensus on which configuration maximally combines reliability, safety and efficiency with an eye towards healthy profit margins for the operator. Studies by [5–11] that provide high-level perspectives using simple models benchmarked on historical data fall short in offering sufficient information to the designer on component performance critical to unearthing some of the nuances that start-ups and other research ventures have encountered at the flight demonstrator phase. Moreover, in most of the aforementioned studies, the energy source of the propulsion network, notably the battery, is characterized at the pack level by an energy density and power density. In so doing, they failed to capture realistic battery behavior and the associated limitations of even the best battery cells available on the market today. With batteries proving to be the enabling technology for EV certification, battery modeling must become a important component in early conceptual design.

This paper seeks to shed light on NASA's campaign to improve advanced aerial mobility and accelerate scalability through the demonstrations of candidate operational concepts and scenarios as summarized in [12]. To the best of our knowledge, there are no published studies that provide a holistic assessment and comparison of conventional electric and VTOL aircraft. This can be largely attributed to the absence of a computational platform that can achieve such a feat. After five years of development, the authors are pleased to present the most recent version release of SUAVE [13], an open-source aircraft design, analysis and optimization environment that is capable of performing such detailed analyses. Although the majority of code development is headed up by the Aerospace Design Lab at Stanford University, there have been noteworthy contributions from industry partners such as Embraer and more recently Exosonic Inc. to expand the code's capabilities. In this study, we deviate from the traditional, oversimplified approaches and move in the direction of higher fidelity techniques to provide realistic expectations of vehicle performance.

To lay the foundation for methodologies discussed later in this paper, an overview of the regional and urban air ecosystem is presented in Section II. This includes a summary of proposed use cases of eS/VTOL aircraft as well as potential mechanisms stalling market feasibility. In section III, the classification of aircraft based on physical attributes is formalized and more details regarding the aircraft modeled in this study are given. A review of mission specifications

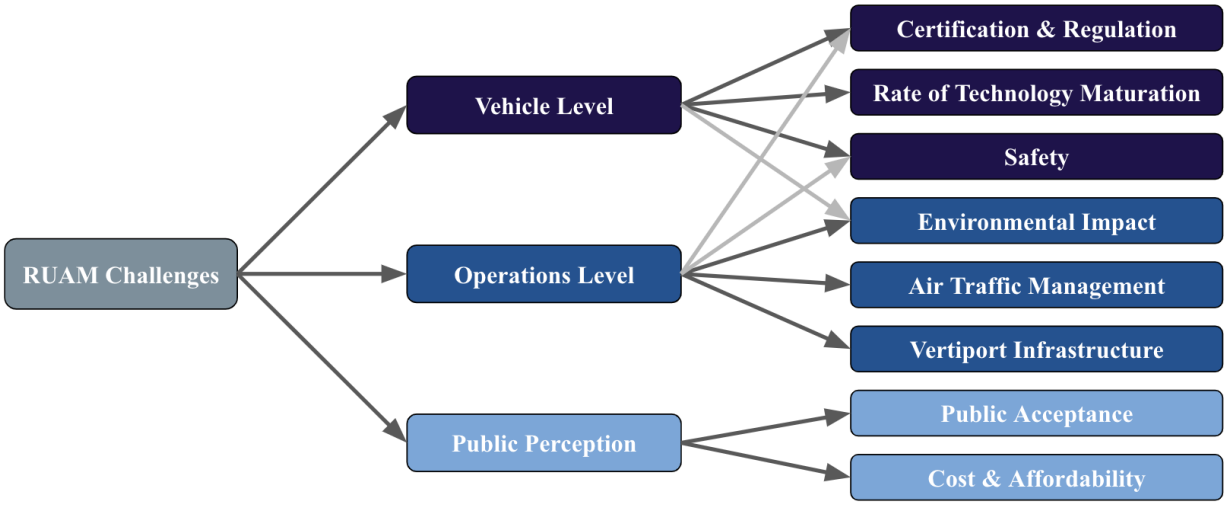

Fig. 1 Market feasibility challenges of the future regional and urban air mobility ecosystem.

required to meet certification standards, performance targets, noise emission constraints and other aspects of operation needed to realize net-positive business revenue is covered in Section IV. In Section V, we outline the analysis techniques and computational models used to assess various attributes of the vehicle from aerodynamics to weight estimation. This is followed by subsystem component sizing in Section VI. A thorough discussion on the performance of these aircraft is documented Section VII, after which concluding remarks on the impact of design choices such as a change of flight profile, passenger capacity and battery cell cathode chemistry is provided in Section VIII.

II. The Regional and Urban Air Mobility Ecosystem

Operating between the outer confines of suburbs and densely populated metropolises, eS/VTOL aircraft are expected to offer advantages in both speed and range compared to personal vehicles, rideshare services and public transportation [14, 15]. Though intended for on-demand commuter travel, it is the view of some [12] that the de facto adopters would be other peripheral applications such as air ambulances, search and rescue missions, surveillance and commercial cargo delivery. Despite recent technological advances providing the impetus for realizing regional and urban air mobility (RUAM), questions regarding vehicle design, supporting infrastructure, regulations and societal constraints remain unanswered. These challenges can be hierarchically grouped into the domains illustrated in Figure 1. Below, we expand on some of these areas to provide context to the design and optimization choices made in Section VI.

Safety: From cockpit simulation to vehicle deployment, electric general aviation (eGA) and eS/VTOL aircraft must demonstrate a level of safety comparable to present-day commuter aircraft of similar weight class, utility and service ceilings. According to the Bureau of Transportation Statistics [16], this equates to less than a 0.85 percent fatality rate. This rate is computed per 100,000 flight hours. As the public has seen with autonomous cars, any mishap or fatal accident will garner significant attention and retard technology adoption [17].

Rate of Technology Maturity: This is a significant challenge for aircraft designers as they must factor in technology readiness levels into design methodology to ensure rapid turnaround time between initial concepts and scaled prototypes for flight tests. Examples of such enabling technology include batteries and other stored energy cells, collision detection and avoidance systems, airframe composites and human-assisted control architectures for complex flight maneuvers. Market modelers must also factor in the rate of technology improvement when forecasting earning potential. In this paper, special interest is placed on the energy and power densities of lithium-ion battery cells used in many of the EVs on the market today. The cycle and calendar life of these electrochemical cells also has an impact the long-term operations of electric aircraft. This however is not covered in this study.

Environmental Impact: Though RUAM aircraft are envisioned to be more eco-friendly than existing aircraft for short-range travel, life-cycle greenhouse gas emissions that encompass generated charging power at the grid will

significantly increase. Realizing net reductions in emissions will not only require operations at scale to reach carbon neutrality, but collaboration between service providers and state governments to promote renewable energy. Furthermore, both the perceptive (audible) and psychological (psycho-acoustic) impact of these air vehicles will have to be addressed to reach acceptable levels within residential spaces.

Certification and Regulation: This process is typically overseen at the national level by aviation authorities such as the U.S. Federal Aviation Administration (FAA) and the European Aviation Safety Agency (EASA) and involves international partnerships to establish policies. However, with prototype vehicles just now starting to emerge, data from UAM operations is sparse. Consequentially, the progress in drafting regulatory policies has been gradual. While regulations related to piloted passenger aircraft could be straightforward to devise, the allocation of Class B, C and G airspace for VTOL operations will be more challenging.

Air Traffic Management: As urban skies begin to open, eS/VTOL services will start to launch hundreds of vehicles with inexperienced pilots into an already congested airspace with commercial passenger aircraft, rotorcraft for medical emergencies and media and military aircraft operations. Such a scenario will require a complete overhaul of today's air traffic control system to be more coherent and intuitive.

Vertiport and Grid Infrastructure: Apart from the vehicle itself, the establishment of vertiports to accommodate the high volume of aircraft stand as the single largest undertaking by stakeholders. Urban planning and land-use approval can take upwards of three years and the ensuing development encompassing the transformation of buildings, helipads, airports and unused land to serve as takeoff and landing zones for another five years. Additionally, there will need to be upgrades to grid infrastructure to handle power surges during peak times of the day like rush hour.

III. Classification of Electric Aircraft Configurations

The idea of UAM has been around for more than half a century, dating back to the inception of helicopters and turbine engines capable of achieving vertical flight. High operating costs, unbearable noise levels and technology in its infancy that attributed to fatal accidents however brought operators to a grinding halt by the 1980s. Fast-forwarding decades later, social trends such as ridesharing in conjunction with advancements in distributed electric propulsion, battery storage, autonomy and a better understanding of acoustic noise and sound propagation have made it possible to build flight demonstrators and that are quieter, cleaner and more efficient [18].

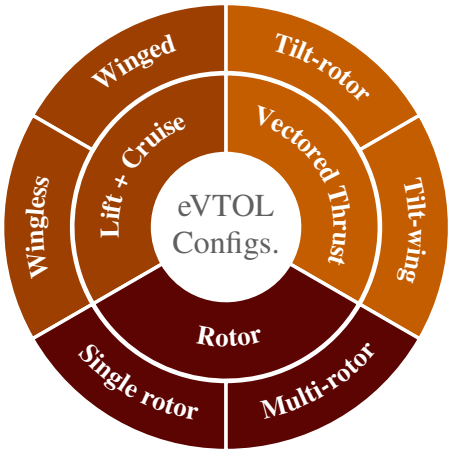

Fig. 2 Classification of eVTOL configurations.

Though there is an infinite number of possibilities for the configuration of an eVTOL, these aircraft can be grouped into three categories based on their distinctive propulsive networks and flight dynamics as shown on the inner ring of Figure 2. As noted by Moore [19], many concepts attempt to leverage the scale-invariant nature of electric propulsion to distribute propulsors around the airframe, offering substantial benefits to control authority and weight-distribution compared to traditional internal combustion engine (ICE) or turbine-driven propulsion. Secondly, compared to ICEs, electric motors have a wider RPM envelope in which near-optimal torques and efficiencies can be maintained, reducing the cost that comes with the complexity of variable pitch propellers [20].

Lift+cruise eVTOLs have separate systems for the vertical climb and forward thrust. The transition between hover and cruise is managed through the coaction of these two propulsive networks. Vectored thrust eVTOLs, which include tilt-wing, tilt-prop and tilt-fan aircraft use the same propulsion system for hover, transition and cruise. This multi-purposing of a single propulsive networks oftentimes leads to compromises in performance even in the presence of gearboxes or variable pitch mechanisms. It must also be mentioned here that both lift + cruise and vectored thrust eVTOLs can be wingless or have wings for more efficient cruises. The third major classification is rotary-wing eVTOLs, which can be further subdivided based on the number of main rotors, that is, single or multi-rotor. Despite possessing attractive VTOL characteristics, these aircraft are limited in airspeed by the speed of the advancing blade speed in

edgewise flight. To reduce vehicle footprint for all three of the aforementioned configurations, VTOL designers may opt for coaxial rotors to achieve thrust requirements. This nonetheless comes at the expense of aerodynamic efficiency.

The examination of an eGA and eVTOLs signifying the major categories described above is undertaken in this current study. These eVTOLs are a stopped-rotor, tandem tilt-wing and multi-rotor aircraft. Inspiration for the four aircraft was taken from tech-demonstrators in existence today, notably NASA's X-57 Maxwell Modification II, Wisk Aero's Cora, Airbus's Vahana and CityAirbus' demonstrators respectively. These aircraft were selected based on the abundance of publicly available geometric parameterizations and subsystem specifications of these aircraft. Renderings of the four aircraft are shown in Figure 3. A full breakdown of vehicle dimensions and powertrain attributes will be provided in Section VI with the sizing methodology.

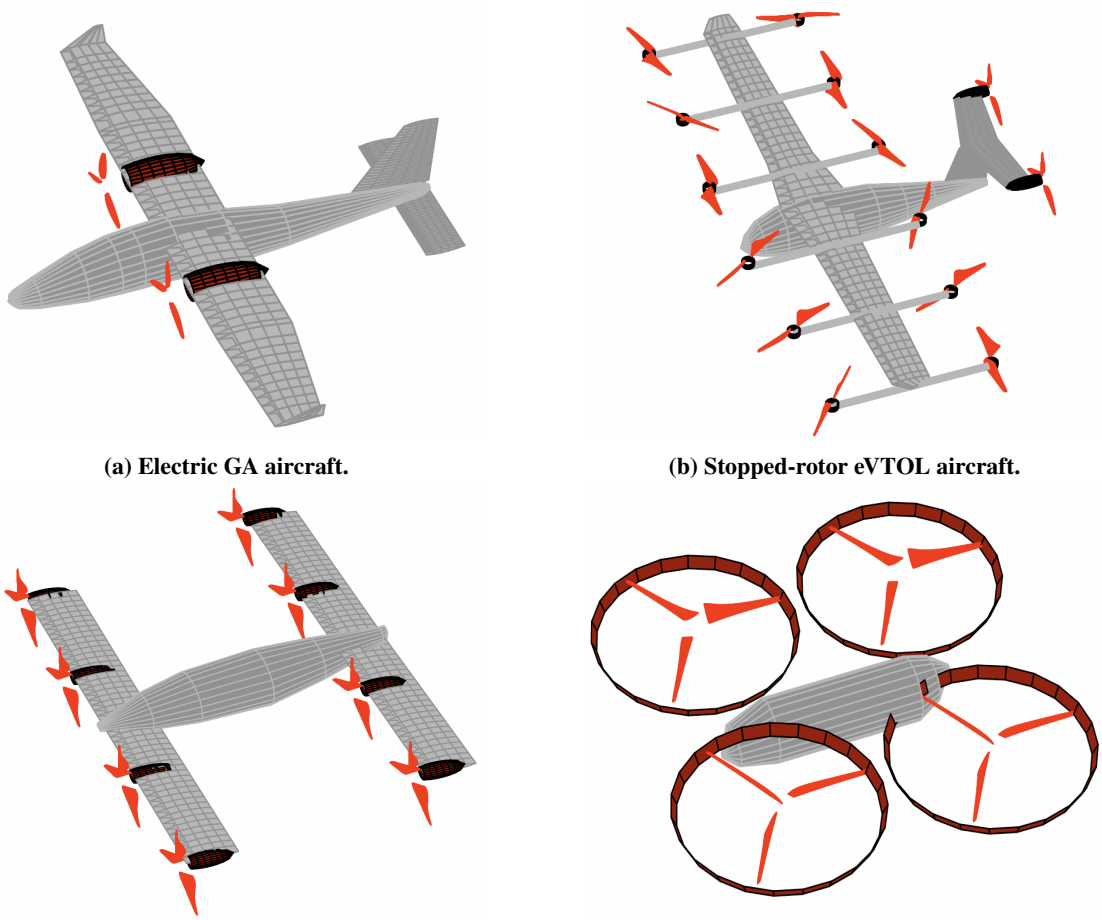

(a) Electric GA aircraft.

(b) Stopped-rotor eVTOL aircraft.

(c) Tandem tilt-wing eVTOL aircraft.

(d) Multi-rotor eVTOL aircraft.

Fig. 3 Aircraft reference models.

IV. Mission Specifications and Flight Profiles

Analogous to the preliminary design stage of conventional tubular and wing aircraft, the development of eS/VTOL aircraft must be preceded by the establishment of operation specifications and performance requirements needed to generate revenue once introduced into market. Adapted from Straubinger [18], Figure 4 identifies these factors, divided into major requirements (dark grey), design drivers (grey) and external boundary conditions (light grey). First, with respect to range, the battery is sized in this study to facilitate a two-leg mission without intermediate recharging as suggested by Patterson [21]. Each leg was 70 nautical miles (nmi). An additional battery reserve constraint was included to demonstrate the ability of the aircraft to reroute in the event of an emergency. The aircraft are designed to accommodate a maximum capacity of 6 passengers or otherwise a payload of 545 kg, with cruise speeds between 75

mph and 175 mph. Preliminary sizing was carried out prior to mission simulations to ensure that the winged aircraft studied were capable of achieving a minimum L/D of 12 at cruise. Additionally, rotors of aircraft with VTOL capability were designed to have disc loadings no greater than 100 lb/ft^2 to keep out of plane structural bending moments on the blade and stresses on the motor within a manageable range. Furthermore, unlike the original diagram in [18], noise is promoted from an external boundary condition to a major requirement to emphasize this metric as a pivotal factor in VTOL certification. In accordance with Uber's landmark study in 2016 [14], an upper threshold of 67 dBA at ground level from a VTOL at 250 ft altitude is used as an evaluation criterion despite being omitted in the sizing in this present study. To ensure that the aircraft are able to fit within the confines of elevated rooftop vertiports and ground-level vertiports in suburban areas, a maximum allowable span of 50 ft was permitted. This is slightly larger than standard helipads with a touchdown and liftoff area (TLOF) of 30 ft [22]. The impact of chemical state changes and thermal fatigue within the battery cell from repeated operations, the broader implications of fleet charging and the cost of maintenance to aircraft are not factored into vehicle design in this study. They however will be an integral part of future life-cycle studies.

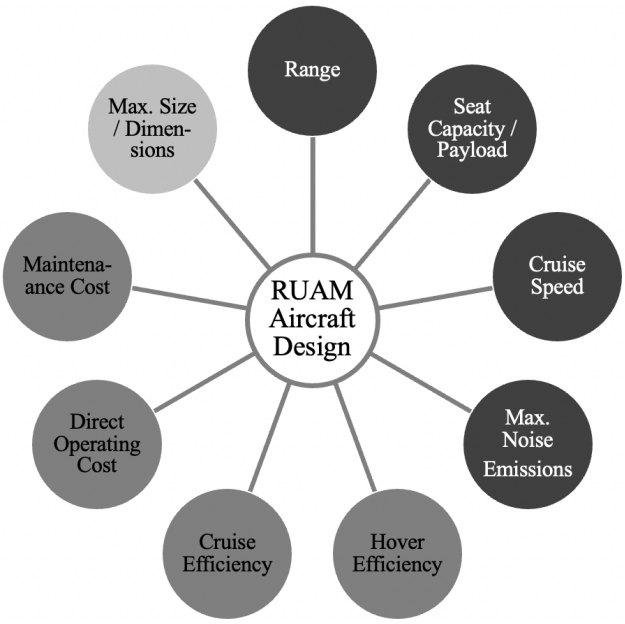

Fig. 4 Design considerations for RUAM aircraft.

With mission objectives in mind, realistic flight profiles that conform to airplane performance operating limits, service ceilings and maximum allowable airspeeds and climbs rate documented in 14 CFR §23 for the eGA and combinations of 14 CFR §23, 27 and 135 for the eVTOL aircraft can now be constructed. Modeling flight paths meticulously, with attention to small details such as aircraft body angle relative to the freestream, enables us to better assess vehicle performance and make well-informed conclusions that warrant serious consideration by current and future aircraft designers. A summary of the mission segments for each vehicle is presented in Table 1 with a more detailed description of the parameters characterizing each segment provided in Table 2. This includes altitude, speed and acceleration for each segment. This is followed by illustrations of the flight profile for the eGA aircraft and the eVTOL aircraft in Figures 5 and 6 respectively.

Table 1 Aircraft Flight Segments.

Segment	GA Aircraft	Stopped-rotor	Tilt-wing	Multi-rotor
1	Takeoff	Vertical Climb	Vertical Climb	Vertical Climb
2	Departure End of Runway	Vertical Transition	Vertical Transition	Vertical Transition
3	Initial Climb Area	Climb Transition	Climb Transition No. 1	Climb
4	Climb	Climb No. 1	Climb Transition No. 2	Cruise
5	Cruise	Climb No. 2	Climb	Descent
6	Descent	Cruise	Cruise	Reserve Climb
7	Downleg	Descent No. 1	Descent	Reserve Cruise
8	Reserve Climb	Reserve Climb	Reserve Climb	Reserve Descent
9	Reserve Cruise	Reserve Cruise	Reserve Cruise	Descent Transition
10	Reserve Descent	Descent Descent	Reserve Descent	Vertical Descent
11	Baseleg	Descent No. 2	Approach Transition	-
12	Final Approach	Approach Transition	Descent Transition	-
13	Landing	Descent Transition	Vertical Descent	-
14	Reverse Thrust	Vertical Descent	-	-

Table 2 Flight Segment Kinematics in SUAVE.

Segment	Symbol	Segment Kinematics
Approach Transition	AT	Constant-Acceleration-Constant-Angle-Linear-Climb
Baseleg	BL	Linear-Speed-Constant-Rate
Climb	CL	Linear-Speed-Constant-Rate
Climb Transition	CT	Constant-Acceleration-Constant-Angle-Linear-Climb
Cruise	CR	Constant-Speed-Constant-Altitude
Departure End of Runway	DER	Linear-Speed-Constant-Rate
Descent	D	Linear-Speed-Constant-Rate
Descent Transition	DT	Constant-Acceleration-Constant-Pitchrate-Constant-Altitude
Downleg	DL	Constant-Acceleration-Constant-Altitude
Final Approach	FA	Linear-Speed-Constant-Rate
Initial Climb Area	ICA	Linear-Speed-Constant-Rate
Landing	L	*Not Modeled*
Reserve Climb	RCL	Linear-Speed-Constant-Rate
Reserve Cruise	RCR	Constant-Speed-Constant-Altitude
Reserve Descent	RD	Linear-Speed-Constant-Rate
Reverse Thrust	RT	*Not Modeled*
Takeoff	TO	*Not Modeled*
Vertical Climb	VC	Vertical Ascent
Vertical Transition	VT	Constant-Acceleration-Constant-Pitchrate-Constant-Altitude
Vertical Descent	VD	Vertical Descent

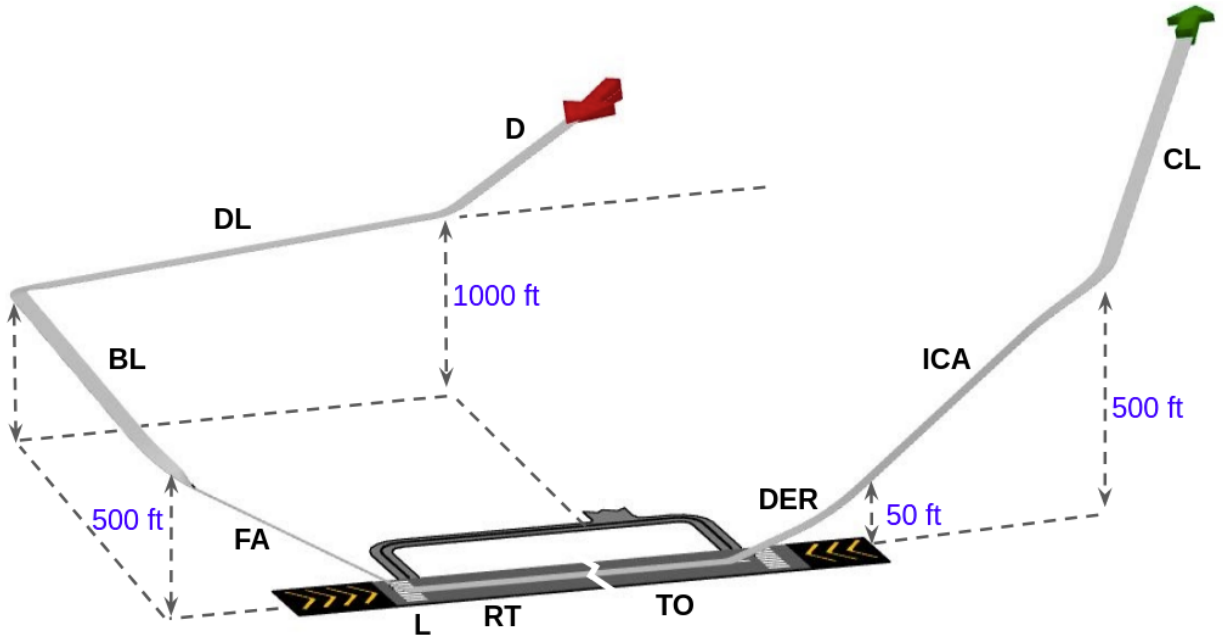

Fig. 5 Typical flight profile of a GA aircraft.

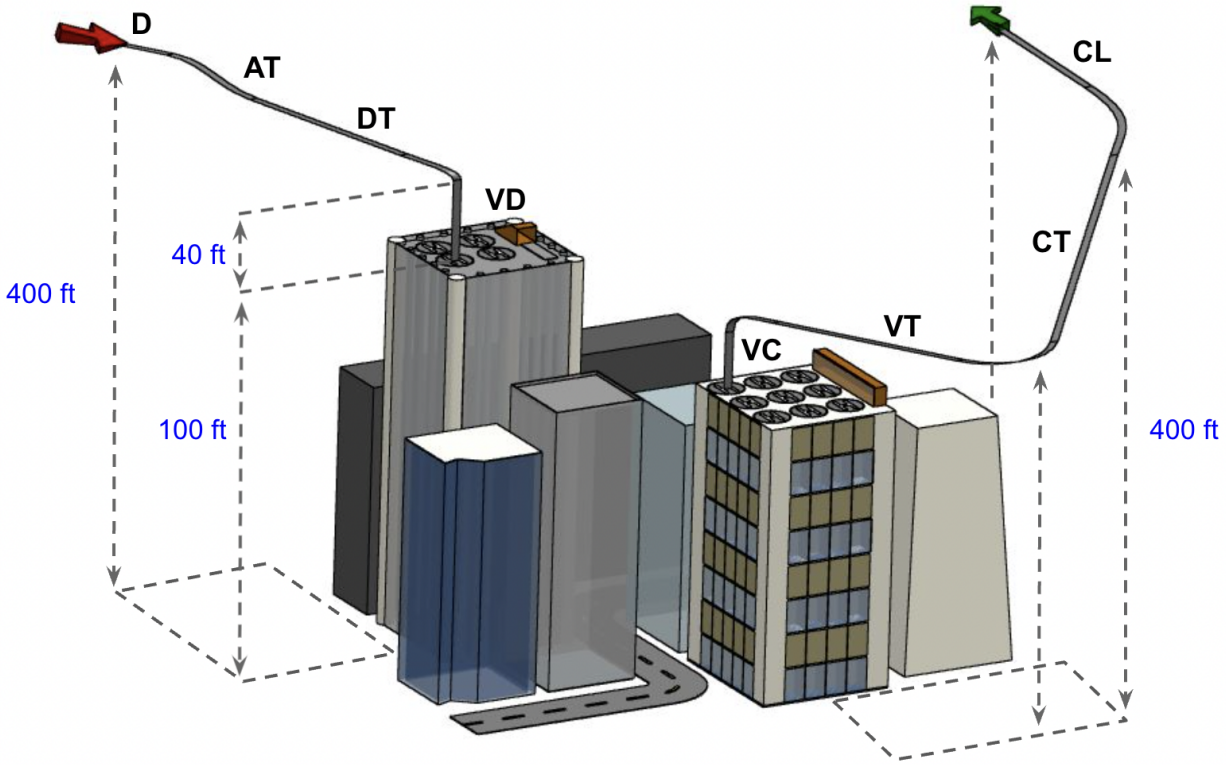

Fig. 6 Proposed flight profile of an eVTOL.

V. Computational Methods For Discipline Analyses

The SUAVE code serves as the simulation platform to evaluate both component-level and system-level attributes of the aircraft in this study. This open-source, python-based tool is modular in architecture, allowing the user to employ varying fidelity levels to design, analyze and optimize vehicles. By this very nature, it is well-suited for both batch large-scale simulations as well as very accurate but computationally expensive simulations. Attributes of a vehicle, represented as data structures, are inherited as python classes conveniently named for generalization. Examples of these classes are wings, propulsion networks, fuselages and other lofted bodies. Furthermore, these classes may contain sub-classes defining other physical components. An example of this is the "*Battery_Propeller*" propulsion network class, which contains the propeller, battery, motor and electronic speed controller sub-classes among others. In this present study, the eGA aircraft is modeled using the "*Battery_Propeller*" propulsion network, the stopped-rotor using the"*Lift_Cruise*" propulsion network, and the tandem tilt-wing and the multi-rotor aircraft both using the "*Vectored_Thrust*"propulsion network.

A flight profile in SUAVE is characterized by pseudo-spectral control points in time and space where the forces, moments, energy and other conservation equations are resolved. The mission solver is designed to allow the aircraft to operate in such a manner that is most efficient at each control point, implying that convergence to a solution can be challenging depending on the initial conditions and whether the rigid-body problem is well-posed and bounded. Oftentimes, simply choosing reasonable values for initial conditions permits the root-finding algorithm from the Scientific Python (SciPy) package used in the solver to arrive at a set of state variables (i.e. angle of attack, propeller rpm, battery current, etc.). A poorly designed component such as insufficient wing area or a low motor K_v will result in the mission solver failing to converge due to no feasible solution. This garbage-in-garbage-out philosophy that SUAVE adopts ensures that designer pays considerable attention to parameterization in the simulation set-up. The following section details the computational approaches employed to simulate some of the main physical components. These models are sequentially run in the mission solver until convergence.

Propulsion Network Model

Propeller Model

Aerodynamic loads and non-dimensional coefficients describing the performance of the propeller and rotor are computed using a Blade Element Momentum Theory (BEMT) model. This model is appealing to conceptual design due to its coupled computational speed and accuracy. Each blade is divided into two-dimensional radial stations as shown in Figure 7 and characterized by a radial location, r, twist angle, chord and sweep (mid-chord alignment). By equating a differential form of the conservation of momentum to the principles of lifting-line theory for rotating blades, the induced velocities at each station can be resolved. The effective angle of attack, as well as the sectional lift and drag components can then be computed and subsequently decomposed into components parallel and perpendicular to the freestream to aquire differential thrust and torque. These can ultimately be integrated along the blade from hub to tip to obtain the total thrust and torque of a propeller or rotor as shown in Equations 1a and 1b.

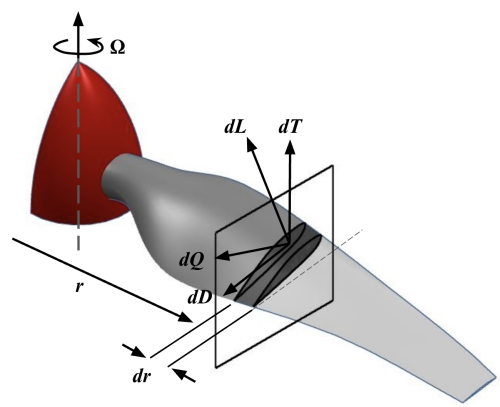

Fig. 7 Sectional forces on propeller blade.

$$T = B\int_{hub}^{tip} T' dr \tag{1a}$$

$$Q = B\int_{hub}^{tip} Q' r dr. \tag{1b}$$

The thrust, torque and shaft power coefficients used to characterize performance are provided below.

$$C_T = \frac{T}{\rho n^2 D^4} \tag{2a}$$

$$C_Q = \frac{Q}{\rho n^2 D^5} \tag{2b}$$

$$C_P = \frac{P}{\rho n^3 D^5} \tag{2c}$$

where

$$n = \frac{\omega}{2\pi}.$$

The propulsive efficiency of converting shaft power to thrust is given by

$$\eta_p = \frac{P_{thrust}}{P_{shaft}} = \frac{Tv}{Q\omega}. \tag{3}$$

The BEMT model implicitly assumes axis-symmetric inflow into the propeller disc making it suitable for a general aviation and lift+cruise configuration. In the case of a vectored thrust aircraft, the use of this model is justified with the stipulation that the transition phase of the flight is slow enough such that the tangential component of the freestream velocity incident on the disc plane is small in comparison to the axial component. For the multi-rotor configuration, this is not necessarily the case as edgewise flight dominates. Here, the half of the rotor where the blade is advancing will have greater lift than the retreating side where the blade is moving in the direction of the freestream. Despite the presence of a Blade Element Theory (BET) model in SUAVE capable of predicting aerodynamic loads that vary around the azimuth of the disc plane, the BEMT model was preferred in this study due to better numerical convergence within the mission solver. Small inaccuracies in the estimation of aerodynamic loads on the rotor for the multi-rotor aircraft are therefore expected.

Electric Motor Model

The motor model used in this study is a simple brushed AC motor model that assumes no loss in latency from switching signs as the internal commutator brushes keep the magnetic fields aligned in the desired phase with the magnets. AC motors tend to be used for high-torque-high-RPM applications where no permanent magnetic field is required, and the electromagnetic field can be adjusted. As a result, these motors have been the preferred choice for both sub-scale and full-sized technology demonstrators. Shown in Figure 8 is a combined illustrative and electrical circuit model. Given the motor speed constant K_v, no-load current I_0, internal resistance R_{0_m}, and the applied voltage V, the torque and power supplied to the propeller at a particular rotation rate can be computed as follows:

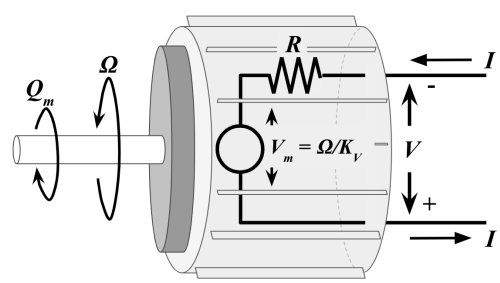

Fig. 8 Electric motor model.

$$Q_m = \frac{(I_m - I_0)}{K_v} \tag{4a}$$

$$\Omega = \frac{(V_m - I_m R_{0_m})}{K_v} \tag{4b}$$

$$P_{shaft} = Q_m \Omega \tag{4c}$$

$$= \frac{I_m - I_0}{V_m - I_m R_{0_m}}. \tag{4d}$$

The efficiency of converting electric energy to mechanical energy is given by:

$$\eta_m = \frac{P_{shaft}}{P_{elec}} = \frac{Q_m \Omega}{I_m V_m} = \left(1 - \frac{I_0}{I}\right)\left(1 - \frac{I_m R_{0_m}}{V_m}\right). \tag{5}$$

In the presence of gearbox efficiency losses represented by η_G and a gear ratio, G, matching the load required by the propeller to the load supplied by the motor resulting in the derivation of motor parameters as functions of the current and terminal voltage. Starting with the manipulation of Equation 4a to derive an expression for motor current, I_m, then substituting into Equation 4d for an expression of shaft power yields:

$$P_{shaft} = \left[\left(V_m - \frac{\Omega}{K_{v_e}}\right)\frac{1}{R_{0_m}} - I_{0_e}\right]\frac{\Omega}{K_{v_e}} \tag{6}$$

where

$$I_{0_e} = I_0 + I_m\left(1 - \eta_G\right) \tag{7}$$

$$K_{v_e} = \frac{K_v}{G}. \tag{8}$$

This is solved for the rotation rate and motor torque by setting the power of the motor equal to the power required by the propeller or rotor to arrive at

$$\Omega = \frac{\left(\pi^{3/2}\right)\left(\left(-16C_p I_{0_e}\rho K_{v_e}^3 R^5 R_{0_m}^2 + 16C_p\rho V_m K_{v_e}^3 R^5 R_{0_m} + \pi^3\right)^{0.5} - \pi^{3/2}\right)}{8C_p K_{v_e}^2 R^5 R_{0_m}\rho} \tag{9a}$$

$$Q = \left(\frac{V_m - \frac{\Omega}{K_{v_e}}}{R_{0_m}}\right) - I_{0_e}/K_{v_e}. \tag{9b}$$

In the above expression, C_p is a vector of power coefficients obtained from the propeller model ran prior in the mission solver at each flight segment defined by the afore discussed control points. Additionally, it is assumed that the motors are connected in parallel, implying that $V_{UL_{bat}} = V_m$.

Aerodynamic Model

A Vortex Lattice Method (VLM) is used to compute the aerodynamic forces subjected on the lifting surfaces of the reference models. This method falls between simple first-order approximations and more computationally-intensive methods such as computational fluid dynamics, thus again earning the classification of a medium-fidelity analysis method. It is capable of producing reasonably accurate predictions compared to higher fidelity methods when benchmarked against experimental data. VLMs are based on lift-line theory whereby the velocity induced at a point C by a vortex filament of length dl is determined using the Biot-Savart law provided in Equation 10a and illustrated in Figure 9a .

In this study, the wings are modeled as mean camber line surfaces and are discretized into panels, with horseshoe vortices whose trailing legs extend from infinity behind each panel and are connected by a bound vortex at the ¼ chord location on the panel. Each wing is modeled with a lattice of 4 panels in the chordwise direction and 16 panels in the spanwise direction. The control point where aerodynamic loads are computed is located at the ¾ chord location of each panel as shown in Figure 9b. The total induced velocity on a control point denoted m on the wing can be determined by numerically integrating the influence of the system of horseshoe vortices on the wing as detailed below in Equation 10b. N is the total number of control panels on the lifting surface. An aerodynamic influence coefficient matrix is constructed from the regular lattice and solved by applying boundary conditions representing flow tangency on each panel to find the strength of the circulation and subsequently the lift and induced drag. This matrix, $C_{m,n}$, depends on the geometry of the nth horseshoe vortex and its distance from the control point of the mth panel. The authors will point the reader to Katz [23] and Bertin [24] who provide well-documented implementations of this method. Integrating over the entire vehicle provides the inviscid aerodynamic coefficients characterizing the aircraft which can subsequently be used along with empirical expressions to estimate viscous and compressibility effects. Corrections to the lift coefficient at high angles of attack as well as details concerning the calculation of parasitic and compressible drag components are outlined in [25].

$$\vec{dV} = \frac{\Gamma_n\left(\vec{dl}\times\vec{r}\right)}{4\pi r^3} \tag{10a}$$

$$\vec{v}_m = \sum_{n=1}^{N}\vec{C}_{m,n}\Gamma_n \tag{10b}$$

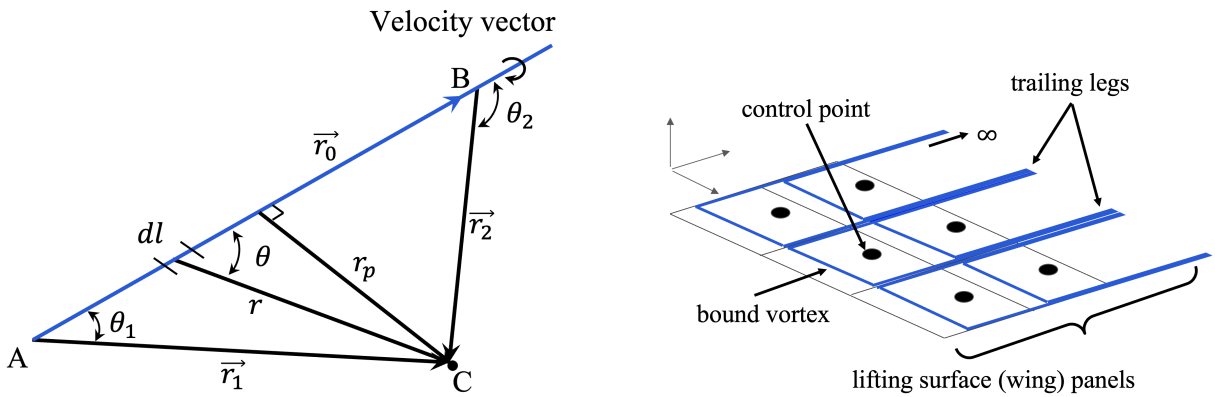

(a) Nomenclature for calculating the velocity induced by a finite-length vortex segment [24].

(b) Representative wing panels, trailing vortices and control points used in the SUAVE-VLM.

Fig. 9 Vortex Lattice Method theory.

Noise Model

The noise model is a post-processing module and is not directly a part of the mission-solving routine. It is therefore not repeatedly computed at each control point but one time after the kinematics of each flight segment are resolved. Once the aerodynamic loads and pressure distributions on the surfaces of the vehicle are obtained, an acoustic signature of the aircraft can be constructed. Excluding the motor, the primary sources of acoustic noise of electric aircraft are (1) rotational noise – occurring at integer multiples of the blade passing frequency and includes thickness noise due to finite blade thickness, P_T and loading noise due to thrust generation, P_L; (2) blade vortex interaction noise – created when rotors blades pass through the wake emanating from another blade; (3) broadband noise – due to turbulent flow impinging on the rotating blades as well as blade self-generated turbulence interacting with the blade trailing edge.

The two main approaches for predicting noise are frequency-domain methods and time-domain methods. The former reconstructs the governing equations using a Fourier transform but has been known to suffer from loss of information as a result of the oversimplification of the blade geometry. However, this loss is less significant for capturing higher harmonics, as pointed out by Hubbard [26]. On the other hand, time-domain methods require large time histories of the pressures from the loading on the blade to compute radiated noise. Although they have demonstrated higher accuracy, these methods are a few orders of magnitude more expensive in terms of wall clock computing time than frequency-domain methods. For the scope of this study, a frequency-domain approach was therefore preferred. Furthermore, only the steady harmonic sources that dominate the noise spectrum are modeled. Broadband components are omitted from the following formulation.

Hanson's formation [27] of harmonic propeller noise in the frequency domain was implemented. Extending from early work by [28–32], this approach encompasses the effects of airfoil thickness, non-axial propeller inflow and blade sweep. The acoustic prediction of the aircraft is confined to rotating blades and excludes fluctuating loads on wings and noise generated in the quasi-steady wake. Starting with a definition of coordinate systems in Figure 10 below, θ and ϕ denote radiation angles of an arbitrary propeller in a freestream at an angle of attack, α relative to the observer. These two angles are defined in Equation 11 along with other geometrical expressions required to fully interpret the diagram.

$$\text{where } \theta = cos^{-1}\left(\frac{x}{S}\right) \quad , \quad \phi = tan^{-1}\left(\frac{z}{y}\right) \quad , \quad S = \sqrt{x^2 + y^2 + z^2} \quad , \quad Y = \sqrt{y^2 + z^2} \tag{11}$$

Applying the required transformation from the visual frame to the retarded frame using Equations 12a and 12b result in the corrected distance and radiation angles from the point of emission.

$$\theta_r = cos^{-1}\left(cos(\theta)\sqrt{1 - M_x^2 sin^2\theta} + M_x sin^2\theta\right) \tag{12a}$$

$$\S_r = \frac{Y}{sin\theta_r} \tag{12b}$$

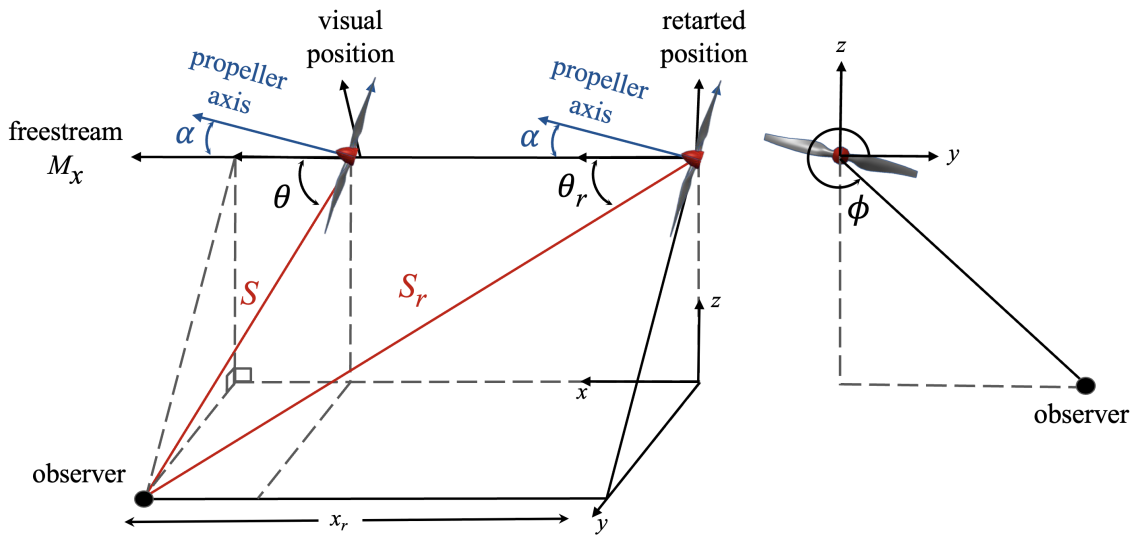

Fig. 10 Sound emission reference frames.

Finally, modification of the propeller from the inertial frame to the body-fixed frame oriented α relative to the freestream as shown in Figure 10 yields the following:

$$\cos\theta_r' = \cos\theta_r \cos\alpha + \sin\theta_r \sin\phi \sin\alpha \tag{13a}$$

$$\cos\phi' = \frac{\sin\theta_r}{\sin\theta_r'} \cos\phi \tag{13b}$$

With these definitions, the thickness and loading noise components of the root mean squared pressure of the nth rotor is be expressed as:

$$P_{m_{T_n}} = \frac{-\rho a^2 B \sin\theta_r \exp\left[imB\left(\frac{\Omega S_r}{a} + \left(\phi' - \frac{\pi}{2}\right)\right)\right]}{4\sqrt{2}\pi(Y/D)\left(1 - M\cos\theta_r\right)} \int_{hub}^{tip} M_s^2(h/b) \exp\left(i\phi_s\right) J_{mB} k_x^2 \Psi_V \, dr \tag{14}$$

$$P_{m_{L_n}} = \frac{imBM_t \sin\theta_r \exp\left[imB\left(\frac{\Omega S_r}{a} + \left(\phi' - \frac{\pi}{2}\right)\right)\right]}{2\sqrt{2}\pi Y r_t \left(1 - M\cos\theta_r\right)} \int_{hub}^{tip} \left[\frac{\cos\theta_r'}{1 - M\cos\theta_r}\frac{dT}{dr} - \frac{1}{r^2 M_t r_t}\frac{dQ}{dr}\right] \exp\left(i\phi_s\right) J_{mB} \Psi_L dr \tag{15}$$

where

$$J_{mB} = J_{mB}\left(\frac{mBrM_t \sin\theta_r'}{1 - M\cos\theta_r}\right) \tag{16}$$

J_{mB} denotes Bessel functions of the first kind of order m and comes through manipulation of the governing Ffowcs Williams-Hawking equation in the time domain. m is the harmonic number and B is the number of blades. k_x, the ratio of the blade passing frequency to the speed of the aircraft or wavenumber for short is given as:

$$k_x = \frac{2mBbM_t}{M_s\left(1 - M\cos\theta_r\right)} \tag{17}$$

The phase lag due to the sweep of the propeller, ϕ_s, is defined as:

$$\phi_s = \frac{2mBM_t}{M_s\left(1 - M\cos\theta_r\right)} \frac{MCA}{D} \tag{18}$$

ϕ_s will be of particular interest in future optimizations of both the rotor and propeller blades as blade sweep has a significant impact on the phase of radiated sound and the onset of the critical blade tip Mach number. The effect

of chordwise non-compactness is captured through non-dimensional source transforms Ψ_V and Ψ_L, which will be examined in succeeding studies. Given below in Equation 19 and 20, the first term approximates the chordwise thickness as a parabolic distribution with maximum thickness at unity while the second represents a uniform lift distribution. Though suitable for conceptional design, a reformulation to accommodate more accurate shape functions will enable topology optimization using a frequency-domain acoustic prediction approach.

$$\Psi_V\left(k_x\right) = \begin{cases} 2/3 & \text{if } k_x = 0 \\ \frac{8}{k_x^2}\left[\frac{2}{k_x}\sin\left(\frac{k_x}{2}\right) - \cos\left(\frac{k_x}{2}\right)\right] & \text{if } k_x \neq 0 \end{cases} \tag{19}$$

$$\Psi_L\left(k_x\right) = \begin{cases} 1 & \text{if } k_x = 0 \\ \frac{2}{k_x}\sin\left(\frac{k_x}{2}\right) & \text{if } k_x \neq 0 \end{cases} \tag{20}$$

The total unweighted sound pressure level from a single rotor is determined through decibel arithmetic as follows:

$$SPL_{m_n} = 20log\left(\frac{P_{m_{Tn}} + P_{m_{Ln}}}{P_0}\right). \tag{21}$$

The A-weighting scaling to account for human perception is then applied. This expression provided in Equation 22 was developed by first fitting the A-weighting standard to a continuous polynomial. It is then summed to the sound pressure level of the corresponding frequencies to produced a re-scaled noise spectrum.

$$R_A(f) = \frac{12194^2 f^4}{\left(f^2 + 20.6^2\right)\sqrt{\left(f^2 + 107.7^2\right)\left(f^2 + 737.9^2\right)}\left(f^2 + 12194^2\right)} \tag{22a}$$

$$A(f) = 20\log_{10}\left(R_A(f)\right) - 20\log_{10}\left(R_A(1000)\right) \tag{22b}$$

$$SPL_{m_n}(dBA) = SPL_{m_n} + A_f(f) \tag{22c}$$

where f denotes the vector of frequencies of the first 20 harmonics, that is, $f = 2\pi m\Omega B$, $m = 1, 2...20$. The sound pressure level of one rotor is is determined through decibel arithmetic of the A-weighted spectrum at an observer location as depicted in Figure 11a using Equation 23 below.

$$SPL_{tot} = 10log\left(\sum_{i=1}^{i=m/n_{rot}} 10^{\frac{SPL_i}{10}}\right) \tag{23}$$

The total A-weighted sound pressure level of the aircraft can be similarly computed by summing over the various sources at each observer location. These observer locations are positioned in the inertial frame on the x-y plane beneath the aircraft, confined to a 45° vertex angle from the negative z-axis as shown in Figure 11b. This suggests that as the aircraft gains altitude, the covered array of observer locations expands in footprint.

Vehicle Weight Estimation Model

Takeoff gross weight (TOGW) is a critical design parameter to consider in the evaluation of mission feasibility. This is especially true for aircraft with VTOL capability where distributed weight not only dictates initial vertical climb but transition maneuverability of the aircraft. For conventional aircraft, historical data and high-level geometry parameterizations may be sufficient to directly ascertain component weights from the regression. For emerging eVTOLs, these historical correlations fail for several reasons listed by Smart [33]. It was therefore necessary to use a more physics-based approach. With the exception of motors and smaller avionic systems, this current study utilizes a component-by-component, loading-driven weight build-up of the vehicle weight implemented in SUAVE. The authors will refer the reader to the code repository on GitHub [13] for the full description of this methodology. This flexible build-up method considering novel classes of vehicles rely on projected aerodynamic loads, material properties and safety criteria to drive the sizing of components. This approach also grants the ability to incorporate new information as it emerges.

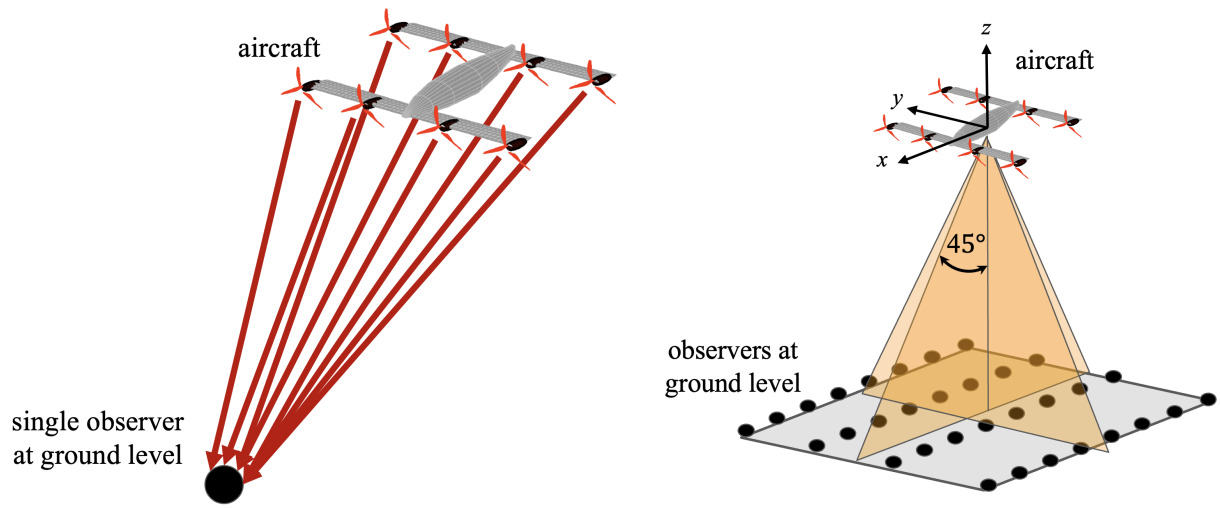

(a) Propagated sound from sourced to one observer.

(b) Observer array locations.

Fig. 11 Source-observer diagram.

VI. Configuration and Component Sizing

The aircraft are designed to a capacity of 6 passengers or a payload of 545 kg, with a cruise speed of 175 mph for all aircraft except the multi-rotor eVTOL that has a cruise speed of 75 mph due to configuration limitations discussed in previous sections. Given the flight profiles detailed in Section IV, the following sub-optimizations were carried out to meet the battery energy targets.

Wing Sizing

Main wings were sized to achieve a minimum L/D of 12 at cruise speed and altitude. This optimization was performed on the clean wing planform, neglecting boundary layer interference of booms and nacelles. To minimize the number of design variables in this sub-optimization, wing area, aspect ratio, root twist and tip twist were the only design variables used the defined the wing planform. All other geometric parameters were determined through the following assumptions: (1) linear twist from wing root to wingtip; (2) ratios of wing chord segments along the wing are held fixed; (3) percent location of wing segments are held fixed in the spanwise direction. The remaining design variables included the location of all lifting surfaces, x_{w_i}, relative to the nose of the aircraft. This includes main wings, tandem wings, v-tails and horizontal tails depending on the configuration. Collectively, these design variables are denoted by $\vec{X}_{wing}$ below in Equation 24. The center of gravity (c.g.) location is updated each iteration by resolving the moments about a reference point. As previously mentioned, the additional constraint of aircraft footprint was included in this optimization ensure that to generated certifiable aircraft are able to operate with existing helipad infrastructures.

$$\begin{aligned} \min_{\vec{X}_{wing}} \quad & C_D(\vec{X}_{wing}) \text{ where, } \vec{X}_{wing} = [S_{ref}, AR, \theta_r, \theta_t, x_{w_i}] \\ \text{s.t.} \quad & L = TOGW \\ & L/D \geq 12 \\ & x_{fp} \leq 50\ ft \end{aligned} \tag{24}$$

Propeller and Rotor Sizing

The propellers were sized to produce the thrust required at transition or cruise conditions depending on the aircraft while rotors were sized to meet the thrust required in hover. To account for a one-engine inoperative (OEI) scenario that could occur due to motor failure or in the event of a bird strike, the rotors were sized to lift a total weight of the aircraft, divided by one less of the total number of rotors. The other two constraints in this optimization were that of disc loading and tip Mach number. Arriving at the optimal blade geometry was achieved using an adaptation of the methodology developed [34] for designing propellers with minimum power losses. Modifications worth mentioning are

a relaxation of the small-angle approximation and the inclusion of sectional airfoil data that accounts for stall as well as compressibility and skin friction drag. In this optimization, the design variables, collectively denoted $\vec{X}_{prop}$ and $\vec{X}_{rot}$ below, are blade radius, chord distribution and twist distribution. The hub fraction is held constant at 10 % of the radius of the blade. The optimization problem is set up for propellers and rotors respectively below:

$$\begin{aligned} \min_{\vec{X}_{prop}} \quad & P(\vec{X}_{prop}) \text{ where, } \vec{X}_{prop} = [r, \Theta_r, \mathbf{c}_b] \\ \text{s.t.} \quad & T = \frac{C_D \frac{1}{2}\rho V^2}{n_{prop}} \\ & DL \leq 100\, lb/ft^2 \\ & M_t \leq 0.6 \end{aligned} \tag{25}$$

$$\begin{aligned} \min_{\vec{X}_{rot}} \quad & P(\vec{X}_{rot}) \text{ where, } \vec{X}_{rot} = [r, \Theta_r, \mathbf{c}_b] \\ \text{s.t.} \quad & T = \frac{TOGW}{n_{rot} - 1} \\ & DL \leq 100\, lb/ft^2 \\ & M_t \leq 0.6 \end{aligned} \tag{26}$$

Electric Motor Sizing

The approach to sizing the motor is outlined in Equation 27 below in which the objective is to minimize the current drawn from the battery while meeting the design torque from the preceding propeller sizing optimization and a target efficiency. The design variables are motor speed constant and internal resistance. Battery voltage, motor RPM and no-load current are fixed parameters and should be chosen by the designer based on power requirements. The philosophy behind such an approach is the projection that the electric motor market will advance to the point where new materials will enable motors to meet the required specifications of the powertrain.

$$\begin{aligned} \min_{K_V, R_{0_m}} \quad & \left(V - \frac{\Omega}{GK_v}\right) / R_{0_m} \\ \text{s.t.} \quad & \left[\left(V - \frac{\Omega}{GK_v}\right) / R_{0_m} - I_o\right] / K_v = Q_m \\ & \left(1 - \frac{I_0 R_{0_m}}{V - \frac{\Omega}{GK_v}}\right)\left(\frac{\Omega}{GVK_v}\right) = \eta_m \end{aligned} \tag{27}$$

Battery Pack Sizing

The battery packs were sized to close the missions outlined in Section IV. That is, they are sized to facilitate two 70 nmi legs. By using lithium batteries available on the market today as opposed to fictitious cells with amplified performance, we ensure that our predictions are grounded in verisimilitude, departing from prior studies that over-estimate energy and power densities. With the steady development of high energy and power density cells, lithium-ion batteries are leading the race to be the energy storage of choice for electric aircraft. Lithium-nickel-cobalt-aluminum oxide (stoichiometry: LiNiCoAlO2, abbreviated NCA) and lithium-nickel-manganese-cobalt-oxide (stoichiometry: LiNiCoAlO2, abbreviated NMC) chemistries are the most common cells used in EVs today. In this study, the NMC cell manufactured by Panasonic[35] was selected. Properties of this cell are provided in Table 3. The optimization of the number of cells required to facilitate the mission including the reserved is given below.

NMC Cell & Pack Parameters	
Property	**Value**
mass (g)	48
height x diameter (mm)	65.3 x 18.5
density (kg/m^3)	1760
specific heat (J/kgK)	1108
nominal voltage (V)	3.6
nominal capacity (Ah)	3.55

Table 3 NMC 18650 cell properties.

As suggested by [36], a tech factor of 1.42, or 42% pack overhead mass fraction is used to account for the mass of the BMS, wiring and protective module housing.

$$\begin{aligned} \min_{\vec{X}_{bat}} \quad & TOGW(\vec{X}_{bat}) \text{ where, } \vec{X}_{bat} = [n_s, n_p] \\ \text{s.t.} \quad & Range_{EOF} = Design\ Range^* \\ & SOC_{fin} \geq 0.1 \\ & C \leq 30 \end{aligned} \tag{28}$$

The state of charge, SOC, is defined as the energy remaining within an individual cell or entire battery pack as a percentage of its fully-charged state. As SOC of 1 corresponds to a fully charged battery. (*) is used above to signify the intended design range for sizing. As will be discovered the following section, meeting this target is configuration dependent.

VII. Comparison of Electric Aircraft Configurations

Until recently, the true potential of SUAVE for designing non-conventional aircraft had not been fully unveiled. That being said, this capability to critically assess the performance of specific components right up to the system-level comes as a double-edged sword. On one side is the ability to attain a deeper understanding of nuanced component interactions at the sub-system level. On one other side are the challenges pertaining to numerical convergence encountered when using physics-based approaches to model complicated dynamics like a transition maneuver. An approach such as this which produces nonsensical results, for instance negative propeller thrust or torque (windmilling), is however extremely useful for creating multi-dimensional Jacobians and Hessians used by the mission solver at the pseudo-spectral control points. It is also advantageous in gradient-based optimization algorithms with a large set of design variables. The garbage-in-garbage-out philosophy of SUAVE ensures that any shortcomings in sizing or difficulties encountered by the mission solver attempting to arrive at a set of state variables, that is, combinations of throttle and angle of attack to produce the forces required to perform the specified flight segment, are highlighted. Here, throttle is defined as the ratio of commanded thrust or power. A throttle setting of one represents full thrust. However, due to non-linearities in the powertrain and flight conditions, the throttle may not be a linear representation of thrust. Provided in the following subsections is a summary of the findings unearthed in vehicle sizing as well as a cross-examination of the first leg of the four aircraft missions.

Aircraft Weight

Beginning with the summary of vehicle specifications in Table 4 and the subsequent donut charts documenting weight breakdown in Figure 12, it can be observed that battery mass is a sizable fraction of TOGW, ranging from 35% of the eGA to over 60% of the multi-rotor aircraft. This discovery conveys that for electric aircraft powered by battery packs comprising these types of cells, the rate of battery technology development stands out as the most critical factor, outweighing other powertrain components such as the evolution of motors and rotor blade design. This also implies that battery weight distribution and location play an important role in vehicle flight stability. The nature of EV battery packs to be arranged in modules that can be positioned around the vehicle as opposed to being situated in one location as a lumped mass does offer some consolation. Aerodynamicists and structural engineers can therefore reposition individual modules to achieve desired static and dynamic stability characteristics to achieve simpler flight control laws and reduce the need for large control surfaces or actuators that add additional weight. Other significant contributors to overall weight of the four aircraft were the motors (in light cyan), wiring (dark green) through the fuselage and wings to power propulsors, passengers (red), fuselage and booms if present (brown) and wings (yellow).

Mission Closure, Battery Energy and System Power Characteristics

Provided in this subsection is a thorough overview of the performance of the four aircraft. In the following figures, the flight time on the x-axis is normalized by the total time for each respective vehicle, $\hat{t} = t/t_{EOF}$. This enables the grouping of data from flight simulations of the four aircraft into a reduced number of figures for the purposes of this paper. The first observation that the authors would like to point out to the reader is the small differences in the flight profiles. The different segments that each aircraft perform on departure and then again on arrival as documented in Table 1 is accredited for this. By accurately modeling maneuvers that follow tightly regulated routes through urban

Table 4 Vehicle Configuration Parameters

	General Aviation	Stopped-rotor	Tilt-wing	Multi-rotor
		General Characteristics		
Capacity (pass.)	6	6	6	6
Length (m)	8.28	6.46	6.1	5
Wingspan (m)	11.4	14.11	9.6	-
Reference Area (m^2)	14.76	16.097	21.7	-
TOGW (lbs)	3968	5511	4850	5726
Battery Capacity (MW-hr)	0.12	0.23	0.23	0.41
	$120s \times 80p$	$150s \times 120p$	$150s \times 120p$	$180s \times 180p$
Powerplant	2 propellers w/ 52.7 kW motors	2 propellers w/ 222 kW motors 12 rotors w/ 195 kW motors	8 rotors w/ 248 kW motors	4 rotors w/ 414 kW motors
Propeller Diameter (m)	1.93	2.3	-	-
Rotor Diameter (m)	-	2.3	2.4	4.2
		Performance		
Cruise Speed (mph)	175	175	175	75
Maximum Operational Altitude (ft)	14000	5000	5000	2500

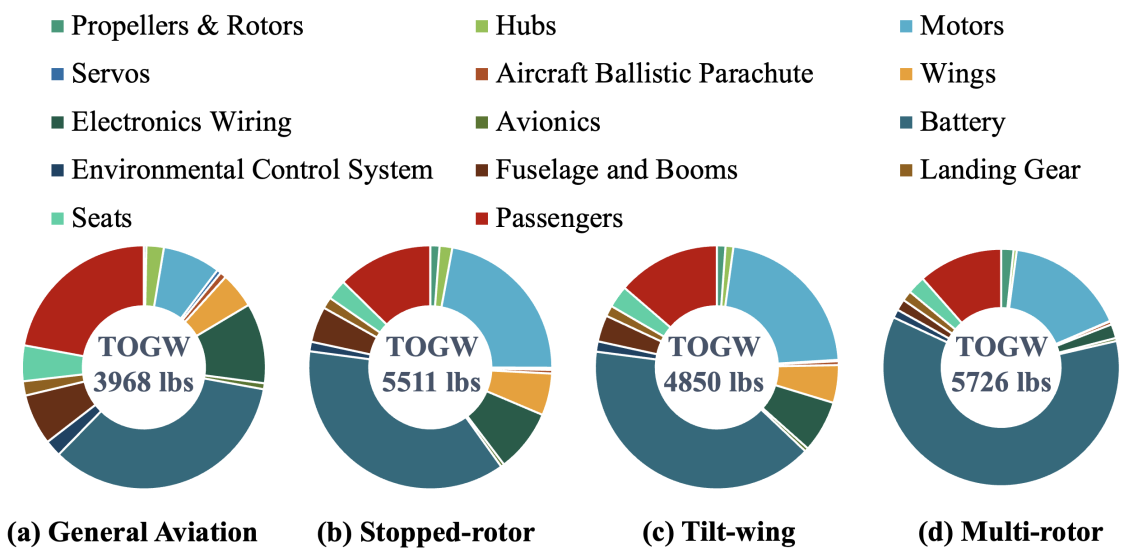

Fig. 12 Electric aircraft weight breakdown.

canyons – tall buildings where wind gusts, updrafts and rapidly changing air currents prevail – no-fly zones for public safety and restricted airspace to reduce daily life disruption, one can obtain a more informed perspective of the first few minutes of flight. This is portrayed in flat regions of the curves representing the three eVTOLs at the beginning of Figure 13a ($\hat{t} \approx 0 - 0.05$). In comparison, a conventional fixed-wing aircraft like the eGA operating out of regional airports with an open departure path will be able to climb sooner at the onset of ground roll on the runway.

The subsequent stages of climb vary from aircraft to aircraft. For example, the multi-rotor eVTOL uses its rotors mounted at 90° (vertically up) to climb while the tandem tilt-wing eVTOL uses a combination of wings to create lift and

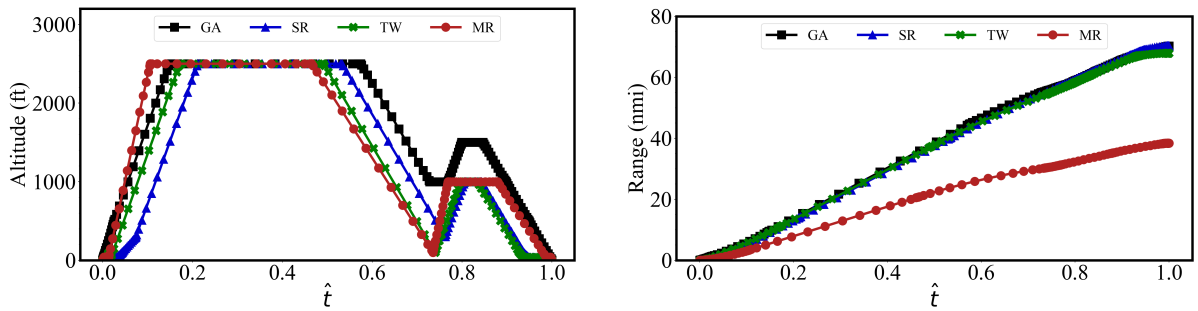

(a) Altitude. **(b) Range.**

Fig. 13 Altitude and range profiles of electric aircraft.

oriented rotors to gain altitude. Because the rotors for these aircraft are designed for a greater window of freestream conditions than those of the lift+cruise eVTOL, the main ascent stages of the flight profile can occur sooner. This is indicated by steeper local gradients in red and green compared to the stopped-rotor's in blue.

Despite its simplistic shape, Figure 13b, together with Figures 14a and 14b convey a common oversight of aircraft designers developing RUAM concepts. The choice of aircraft configuration is a dominant factor in the ability to meet mission requirements defined by market modelers aiming to construct viable business models. Recalling from the previous section, the goal of this paper was to compare the performance of four aircraft operating comparable flight profiles. By inspection of Figure 13b, this is not the case. Three of the four aircraft, the eGA and stopped-rotor and tandem tilt-wing eVTOLs, were able to successfully close the specified mission. That is, the preliminary sizing operations carried out were able to converge to designs capable of reaching a target range of 70 nmi using commercially available lithium-ion batteries. On the other hand, the multi-rotor eVTOL fell significantly short of this range, reaching a maximum distance of approximately 40 nmi. Even with a battery back roughly twice the size of the other two eVTOLs, the multi-rotor aircraft was incapable of performing the 70 nmi mission with net-positive energy. This large difference in range is attributed to the power requirements which wingless aircraft have to sustain to perform altitude changing maneuvers such as vertical climb as well as forward thrust in cruise. With the weight penalty of adding batteries either in series (increasing $I_{bat_{max}}$) or in parallel (increasing $V_{bat_{max}}$), we see that simply increasing the size of the battery pack is nonsensical. Figure 14a provides a clearer interpretation of the size of the battery pack. The conventional tube and wing eGA aircraft has a significantly smaller pack than the stopped-rotor and tilt-wing eVTOLs that both have a 0.23 MW-hr battery pack. As mentioned above, the multi-rotor's pack which is roughly 60% of TOGW has a 0.41 MW-hr battery pack. The associated SOC curves describing the discharge as a function of time are shown in Figure 14b. Here we draw the reader's attention to three local areas denoted ①, ② and ③. They denote the beginning ($\hat{t} \approx 0.05$), the first descent and reserve climb ($\hat{t} \approx 0.8$) and the final descent ($\hat{t} \approx 1$) respectively. The changes in gradient in these regions highlight greater power draw during vertical flight and climb segments. High power loadings of the multi-rotor eVTOL through the flight compared to the stopped-rotor and tilt-wing eVTOLs result in a pronounced drop in SOC. Locating where these drops occur in the discharge curve of a cell is crucial to understanding how system behavior at specific points can prompt phase changes occurring within the electrodes battery cell during cycling.

Figures 15a and 15b relate battery performance to other powertrain components such as rotors, propellers and motors. It has already been established that the climb and transition segments consume more power than cruise and descent segments, however, we can further assess the nonlinear behavior of power consumption throughout the mission as SOC falls. This phenomenon can be more explicitly conveyed via C-rate as shown in Figure 15b. C-rate is defined here as the rate at which the cell's energy is being discharged relative to the remaining battery capacity within the cell. As the energy in the battery pack falls and SOC decreases, there is an associated voltage drop. This voltage deficit leads to the system drawing higher current loads to meet the power requirements of motors and on-board avionics even in constant-airspeed-constant-altitude segments such as cruise. Near the end of the mission in Figure 15b, C-rate can rise as much as 760% of what is experienced in the initial stages of flight. Understanding this phenomenon is paramount from a certification standpoint as engineers developing power electronics must ensure safe operation during repeated use.

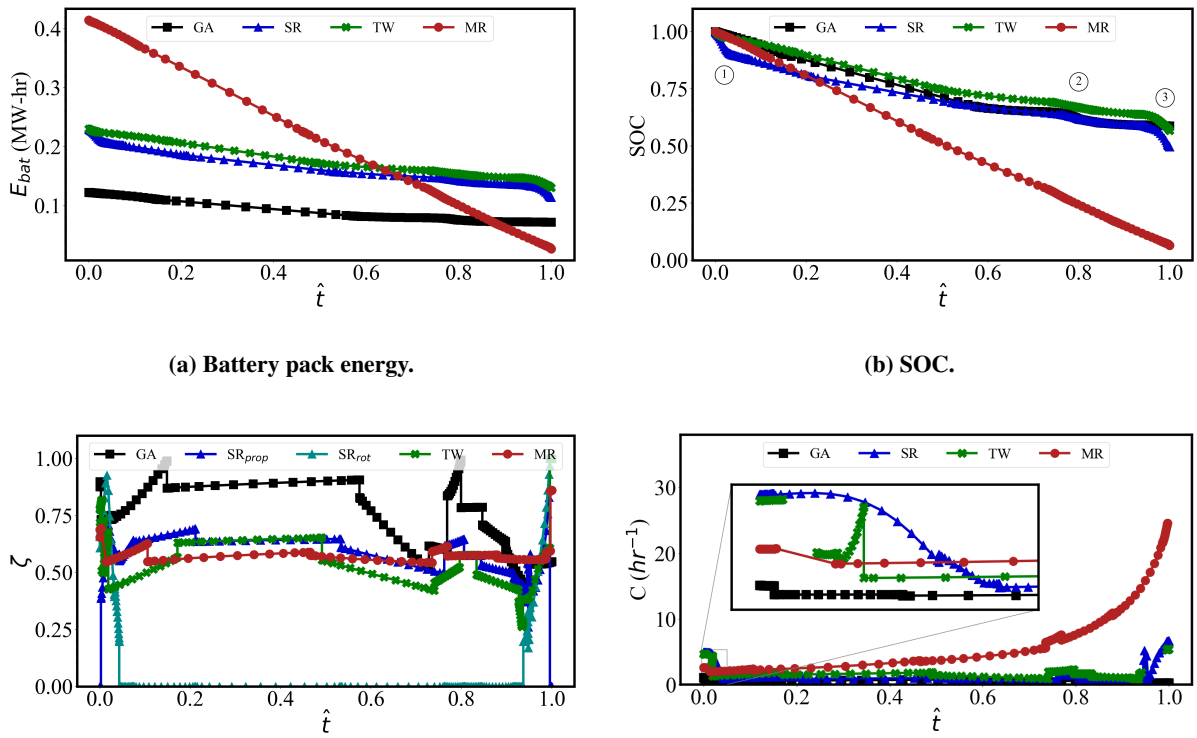

(a) Battery pack energy.

(b) SOC.

(a) Throttle.

(b) C-rate.

Fig. 15 Battery pack performance of eGA and eVTOL aircraft.

Powerplant: Propellers and Motors

Figures 16a to 16d depict motor and propeller performance. The first major takeaway is the realistic variations in RPM captured, allowing the designer to not only discern loads throughout the entire mission but locate specific regions of the flight envelope where undesirable performance warrants further improvement to effect more favorable performance characteristics. An example these modifications is the act of varying blade pitch as airspeed changes to reduce power drawn from the battery, particularly near the end of cycle life. Shown in the two plots in the top row are RPM and corresponding blade tip Mach number. For the stopped-rotor configuration, both the rotors (in teal) for lift and propeller (in blue) are shown. Additionally for this aircraft, note how the rotors throttle down while the propeller throttles from zero to full power as the aircraft accelerates from vertical flight to a forward climb. The plots in the lower row depict how much the thrust and torque loads vary during transition maneuvers compared to more conventional segments such as climb, cruise and descent. By capturing performance in off-design points of the flight profile, these diagrams highlight the importance of component sizing.

Aerodynamics and Flight Mechanics

The following group of plots in Figure 17 pertains to the aerodynamics of the modeled aircraft. Apart from the self-explanatory trends of flight performance depicted in these diagrams, they provide insights central to a profound understanding of the flight mechanics unique to each configuration. The body angle of passengers in each vehicle throughout the entire flight can be attained from Figure 17a. The angle of attack of the eGA aircraft model closely agrees with flight data of an internal combustion engine aircraft of equivalent size. For this aircraft, high angles of attack during the climb and descent phases to generate more lift and an angle of attack around 3° in the cruise validates the computational approaches used in this study. The more unorthodox flight profiles of the three eVTOLs offered alluring takes on the maneuvers performed. They also serve to underscore the unbiased and unconstrained nature of how the root-finding algorithm works within the mission solver to arrive at a set of state variables that satisfy the conservation equations.

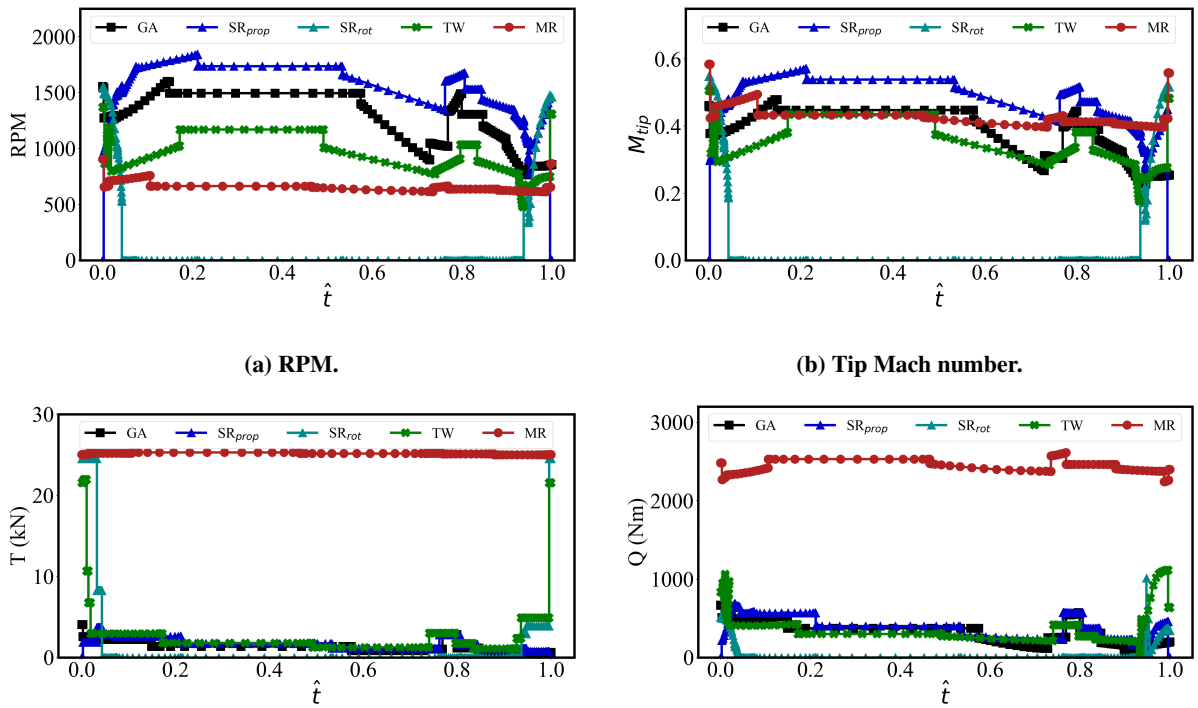

(a) RPM.

(b) Tip Mach number.

(c) Thrust.

(d) Torque.

Fig. 16 Propulsive performance of eGA and eVTOL aircraft.

It must be noted that the angles of attack of the eVTOLs during the hover/vertical climb segments were omitted as they alternate between +/- 90° depending on the motion of the vehicle. This is solely put down to how the AoA variable is computed in SUAVE using body angle and the velocity vector. The multi-rotor and tilt-wing configurations have similar accelerating phases of flight where the aircraft are transitioning out of vertical climbs to a low forward airspeed. During this phase, a downward pitching rotation of these two aircraft is observed as the mission solver orients the rotors in the direction of the positive x-axis to generate forward thrust. Contrasting flight dynamics are observed as these two aircraft gain airspeed. The mounting angles of the wings of the tilt-wing eVTOL adjust to generate more forward thrust. On the other hand, similar to a helicopter in forward flight, the multi-rotor continues to pitch downward to accelerate. This results in negative lift from the fuselage surfaces modeled in the VLM.

In the case of the stopped-rotor in transition, the aircraft tends to pitch up at high angles of attack as the mission solver seeks to orient the vehicle in such a manner to generate lift using both the rotors together with the main wing. At this stage, rotors that are used to produce the initial vertical lift begin to throttle down while the rear propellers throttle up to generate forward thrust. As this aircraft gains airspeed, the angle of attack reduces to cruise values around 2.7°. The observed behavior of the simulated stopped-rotor and tandem tilt-wing aircraft mirror the flight dynamics observed of their respective flight demonstrators built by Wisk [37] and Acubed [38], further validating our preliminary findings. In climb and cruise segments, these two vehicles take to more conventional performances, with recorded L/D values around 14.2 for the stopped-rotor and 12.8 for the tilt-wing aircraft as seen in Figure 17d. These two streamline-bodied eVTOLs have low drag coefficients compared to the multi-rotor with a blunt body resulting in a drag coefficient at cruise around 0.5. This falls in the ballpark of what is expected, given that the drag coefficient of a sphere is approximately 0.5 and a long cylinder 0.82.

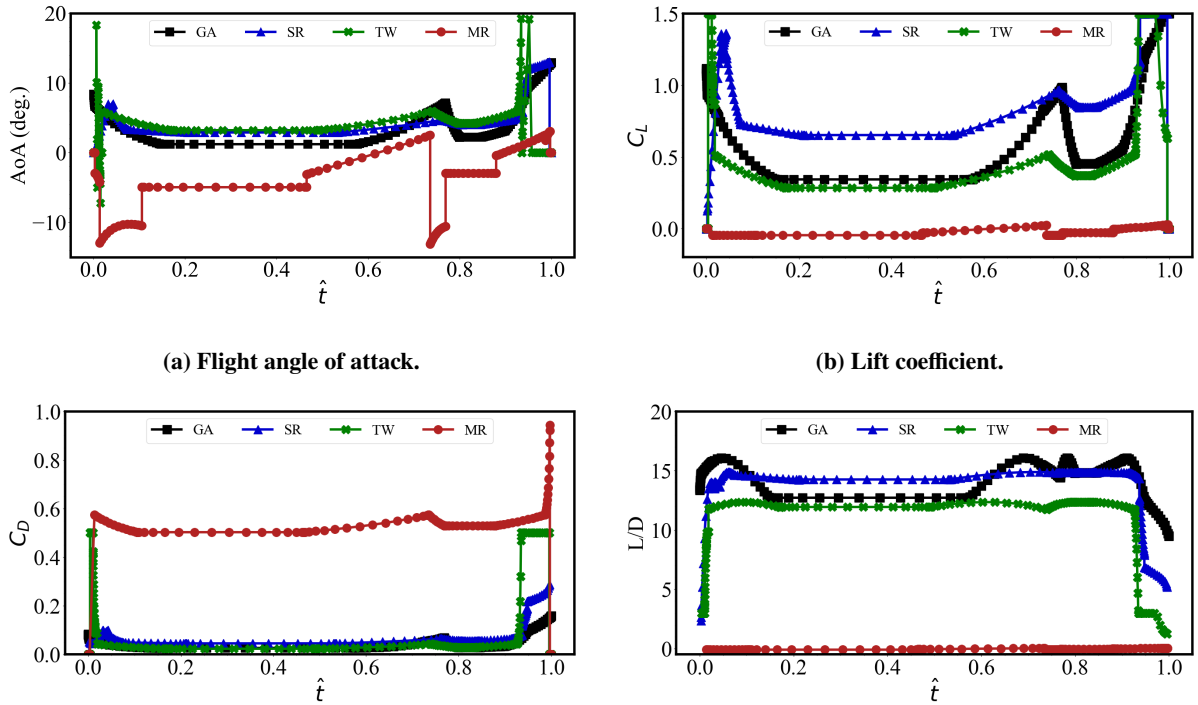

(a) Flight angle of attack.

(b) Lift coefficient.

(c) Drag coefficient.

(d) Lift-to-drag ratio.

Fig. 17 Aerodynamic characteristics of eGA and eVTOL aircraft.

Noise Emission and Acoustic Footprint

Vehicle noise measured from ground level is the final discipline assessed in this paper. To reiterate, only the dominant harmonic noise of the rotating blades is considered here – the components of broadband noise, airframe noise and unsteady-wake noise are neglected in the computation. Figure 18a depicts the A-weighted sound pressure level directly beneath the aircraft throughout the entire mission, i.e. $y = 0, x = 0 \forall \hat{t}$. Discontinuities in each curve correspond to the changes in vehicle orientation that influence noise directivity. The general trends of decreasing noise level as the aircraft gain altitude can be observed whereby the closer the vehicle is to the ground (i.e. initial climb, reserve climb and final descent), the higher the noise level. Lower disc loadings and rotation rates of the multi-rotors lead to this aircraft having the lowest predicted noise levels around 71 around dBA during the nominal and reserve cruise segments. A 3D illustration of acoustic footprint of the stopped-rotor eVTOL aircraft at 250 feet is provided in Figure 18b. No aircraft was however able to reach the decibel target of 67 dBA suggested by Uber.

Contour plots of the four aircraft in Figure 19 highlight a major hurdle facing RUAM. At an altitude of 1500 ft, the recorded sound pressure levels were in the range of 85-96 dBA. Maneuvering at lower altitudes where these aircraft are expected to operate above buildings will result in significantly higher SPL estimates that violate maximum allowable noise levels. This is portrayed in the acoustic footprint plots of Figure 19a and Figure 19b. As urban airspaces begin to open for business and eVTOL services start to launch hundreds of vehicles, noise exposure from low-altitude vehicles is expected to create a lower threshold for annoyance. Premature deployment could have a devastating impact on the future by resulting in local noise ordinances that restrict operations. To realize this form of transportation in large cities such as New York, San Francisco and Los Angeles, aircraft designers and engineers will need to reduce noise signatures or at least shift the dominant frequencies of the radiated acoustic spectrum to a region of lesser annoyance to the human ear. This can be achieved through phasing or rotor phasing, blade loading alteration through topology optimization and acoustic shield using cowlings. Some of these strategies do however come at the expense of propulsive efficiency.

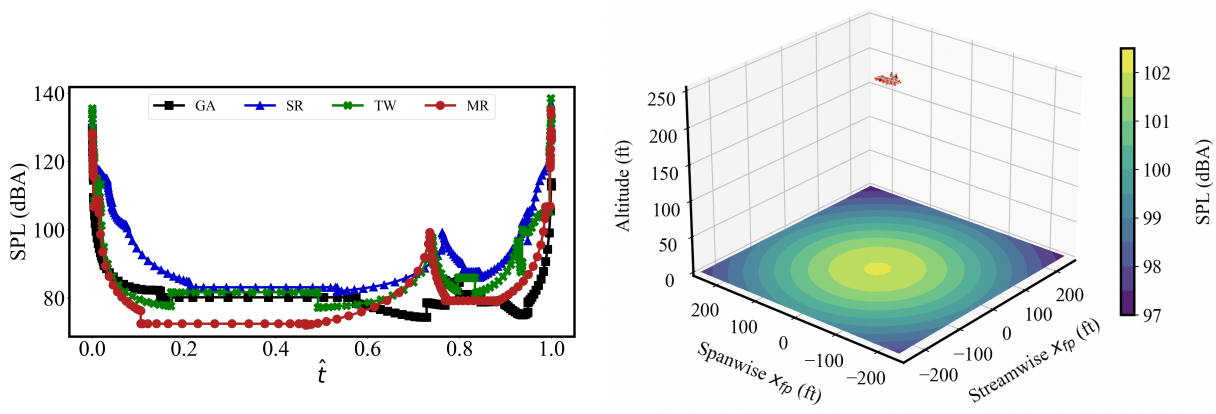

(a) Aircraft noise emissions over full mission. **(b) Stopped-rotor acoustic footprint at 250 ft.**

Fig. 18

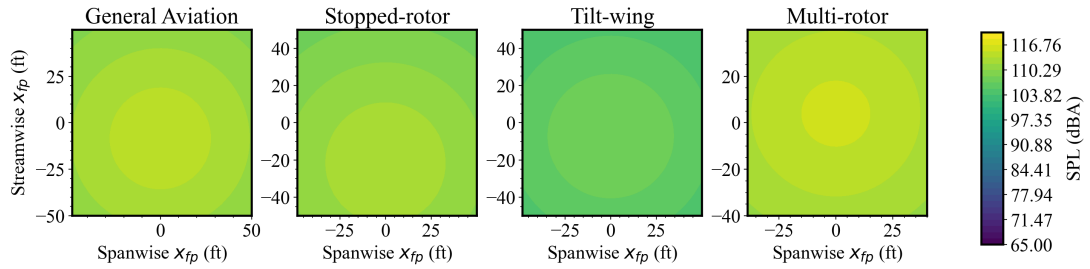

(a) Noise contour at 50 ft.

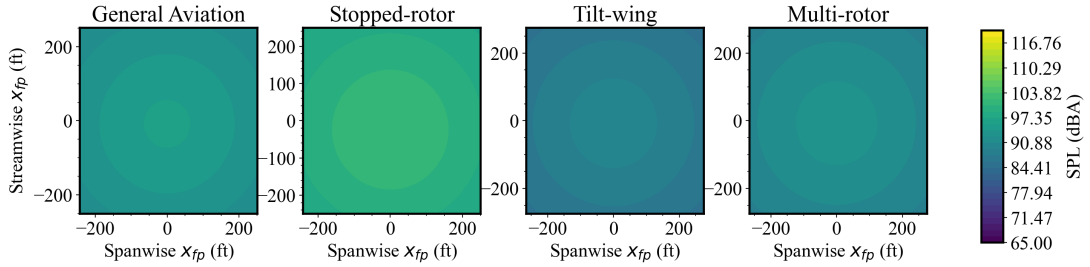

(b) Noise contour at 250 ft.

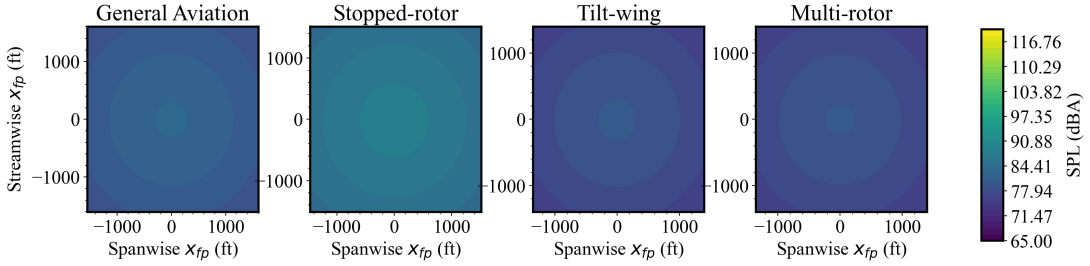

(c) Noise contour at 1500 ft.

Fig. 19 Aircraft acoustic footprint.

VIII. Electric Aircraft Trade Study

The preceding examination of mission requirements, sizing methodology and preliminary results provide a canvas on which we draw conclusions and highlight considerations critical for RUAM electric aircraft design. A review of three domains at the system and sub-component level is covered below.

Battery Cell Cathode Chemistry

As we have seen in this study, the battery is the focal point of feasibility for electric aircraft, particularly those with VTOL capability. In practice, lithium-ion batteries are distinguished by the chemical composition of the cathode used in the cell. The most popular cells on the market today include lithium manganese oxide (LMO), lithium nickel cobalt aluminum (NCA), lithium cobalt oxide (LCO), lithium nickel manganese cobalt oxide (NMC) and lithium iron phosphate (LFP). The anode is typically graphite, however, recent battery development has gone into silica [39] and titanium [40] alloy materials that offer electrochemical stability and reduced corrosive side reactions during idle periods when the cell is not being discharged.

When charging a battery, electrons flow from the cathode through the current collector towards the opposing-pole current collector that is electrically bonded to the anode. The flow of charge through the current collectors outside the battery occurs *in the circuit* and can be easily measured using an ammeter. This is occurs with the movement of lithium ions similarly from the cathode to the anode through the separator electrolyte within the cell causing the density of lithium in the cathode to decrease and that in the anode to increase. During discharge, the reverse occurs whereby electrons flow from the anode to the cathode outside the battery cell while lithium ions migrate from the anode to the cathode inside the cell. This movement of charged particles is accompanied by side reactions that give rise to internal degradation mechanisms, namely solid-electrolyte interface layer growth, loss of anode/cathode active materials, loss of lithium-ion inventory, loss of electrolyte, lithium corrosion, lithium plating, contact loss and diffusion stress [41], which all reduce the battery's stored energy capacity in some manner.

The choice of battery cell therefore dictates the behaviour of the propulsion network. For example, LMO cells have higher energy density and power density, but poor life characteristics while the NMC cells have high energy density but poor safety. LFP on the other hand is the safest cathode and has a long life but suffers from low energy density and low power density making them more suitable for ground-based EVs where weight is not a significant design factor. The NCA cell on the other hand has a the specific energy value of 219 Wh-kg^{-1}, higher than that of alternative cathode materials such as LMO (154.5 Wh-kg^{-1}), LCO (193 Wh-kg^{-1}), LFP (162 Wh-kg^{-1}) and NMC (180 Wh-kg^{-1}) [42] as shown in Figure 20. NCA also has excellent fast charging characteristics, making it attractive to EV applications. However, even with these traits, this cathode material is more expensive to manufacture than NMC [43] – see Figure 21 – resulting in some EV manufacturers making the decision to go for a cheaper alternative. It can be therefore concluded that the design range, intended flight profile, together with aircraft configuration should be factored into the choice of a battery cell.

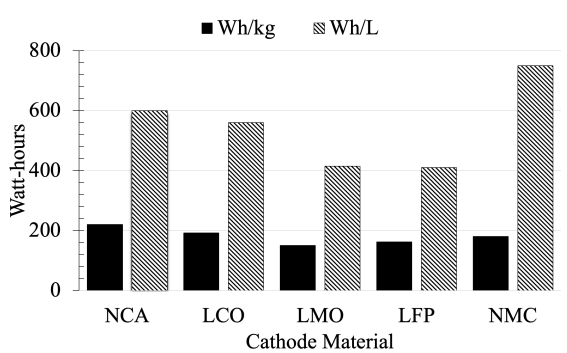

Fig. 20 Comparison of gravimetric and volumetric energy densities of 18650 batteries with commercial and next-generation cathodes [42].

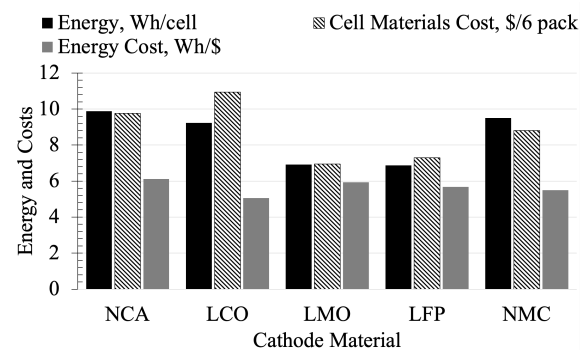

Fig. 21 Energy output and costs of 18650 batteries with targeted cathode materials [42].

Mission Profile

Urban canyons of the future are expected to be heavily regulated due to the presence of existing passenger aircraft, delivery drones, medical airlifts and other communications aircraft, both manned and unmanned operating in the same airspace. Three things can be inferred from the investigation of results in the previous section. The first is that aircraft operating missions with long ranges benefit from having more streamlined fuselage configurations and wings which offer more efficient cruises. Secondly, aircraft with separate powerplants for forward and vertical flight like the stopped-rotor require longer transition times than vectored thrust aircraft such as the tilt-wing eVTOL due to the need to carefully balance forces about the rigid body while avoiding blade and wing stall. Lastly, multi-rotor aircraft have advantages in RUAM applications where vertical flight dominates, for example, helipad to helipad operations between buildings in a city from a noise emission perspective.

Passenger Capacity and Payload Weight

Apart from battery mass, passenger or cargo mass is the largest independent variable of the vehicle weight build-up methodology summarized in Section V. Documented in the SUAVE code is how individual components such as load-bearing structures in the wings, rotors and other subsystems such as the avionics, environmental control and ballistic recovery parachute (BRS) system are sized from passenger and payload weight. This fraction of TOGW is also governed by external factors such as market size, demand and competition. During development and initial testing of the sizing algorithm, it was discovered how sensitive in nature this parameter is to mission closure. In fact, by reducing passenger count to 2, the achievable range of the multi-rotor – provided there is sufficient energy to perform a duplicate return flight – increased by 5 nmi while that of the stopped-rotor and tilt-wing aircraft increased by around 12 nmi. Future work will provide a more quantitative assessment of these sensitivities.

IX. Concluding Remarks

In this paper, we demonstrate the use of medium-fidelity tools and physics-based approaches to design and analyze electric aircraft operating mission profiles symbolic of those envisioned for regional and urban air mobility. Although this approach presents certain challenges related to convergence, the act of using realistic estimates of vehicle weight, including technology limitations and modeling vehicle geometry in great detail allow for a deeper understanding of the interactions between subsystems. Moreover, as shown by the nuances in battery performance throughout the flight profiles, this approach allows for the identification of phenomena that commonly go unnoticed when using simpler models are employed.

From the comparison of aircraft configurations, it was observed that battery technology and noise emission at low altitude emerge as the most significant issues to be addressed if designers hope to reify the integration of electric aircraft into urban airspaces. First, concerning batteries, we see that the weight fraction can be as much as 60 % of total weight. The development of batteries with higher specific energy and specific power is therefore essential for reducing TOGW. With respect to radiated noise, any attempt to reduce the acoustic signature of these aircraft will first require the capturing of all generating sources. This includes rotor-on-rotor wake interactions and unsteady wing loads in a propeller slipstream. This will be the focal point of future studies. Design optimization of these aircraft can subsequently be carried out upon obtaining more accurate predictions of the emitted noise.

Another area of future research is the examination of vehicle stability, principally in transition by way of modeling propeller-motor and rotor-motor combinations around the aircraft as separate systems with unique throttles. This undertaking will be preceded by a reformulation of the mission solver to allow for the use of gradient information which is expected to significantly improve convergence. Lastly, it was previously noted that the impact of cycling and calendar aging on the battery is not considered in this study. Following research will look at the inclusion of mechanistic models that capture some of the chemical state changes occurring within the battery cell together with thermal fatigue from repeated operations.

X. Acknowledgements

The first author would like to thank the core members of the SUAVE development team at Stanford University – Emilio Botero, Racheal Erhard, Jordan Smart and Tim MacDonald – for their contributions towards expanding the electric and VTOL analysis capabilities of the code. Additionally, the authors would like to thank former contributors Carlos Ilário da Silva (Embraer) and Tarik Orra (formerly Embraer) for their implementation of SUAVE's first-generation aircraft noise model that served as the foundation for the newly implemented frequency-domain noise formulation.

XI. Appendix

Provided in this section are isometric drawings of the four aircraft studied in this paper along with the data used to parameterize the flight segments modeled in the respective missions. Results depicted in this report can be reproduced using this information along with version 2.4 of the SUAVE code released in June 2021.

A. Electric GA Aircraft

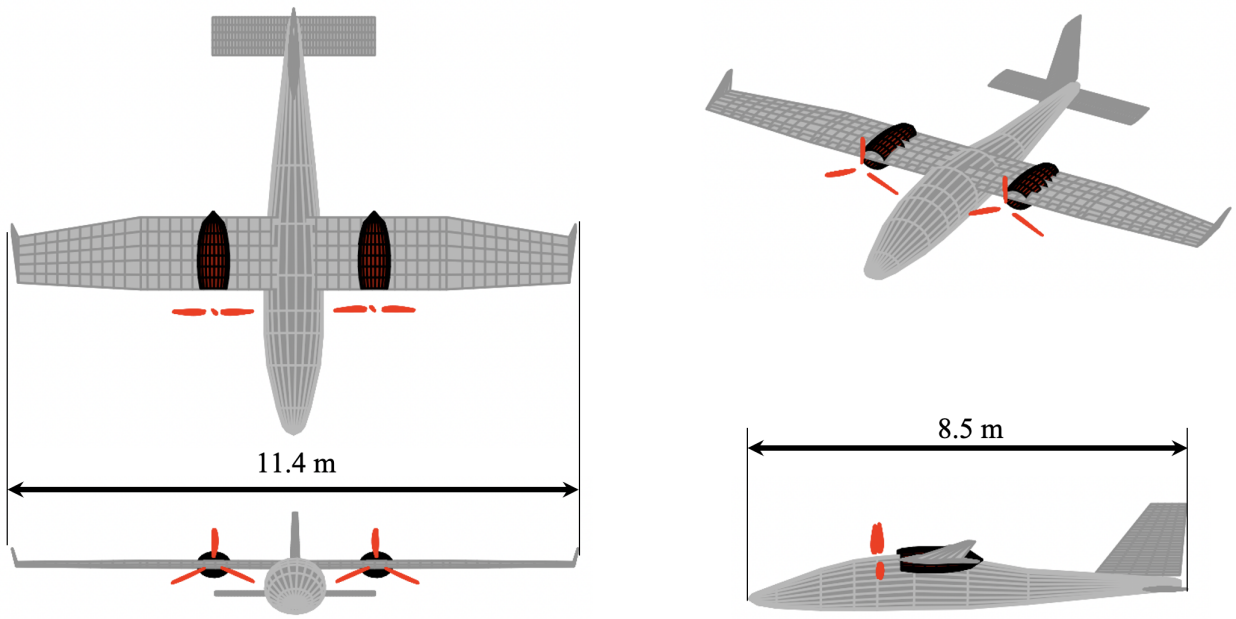

Flight Segment	Initial Altitude (ft)	Final Altitude (ft)	Initial Speed (mph)	Final Speed (mph)	Climb Rate (ft/min)
TO	0	0	0	91	0
DER	0	50	91	100	600
ICA	50	500	100	110	600
CL	500	2500	110	175	500
CR	2500	2500	175	175	0
D	2500	1000	175	50	-300
DL	1000	1000	50	100	0
RCL	1000	1500	100	150	500
RCR	1500	1500	150	150	0
RD	1500	1000	150	135	-300
BL	1500	500	135	90	-300
FA	500	0	90	78	-300
L	0	0	78	50	0
RT	0	0	50	0	0

B. Stopped-Rotor eVTOL

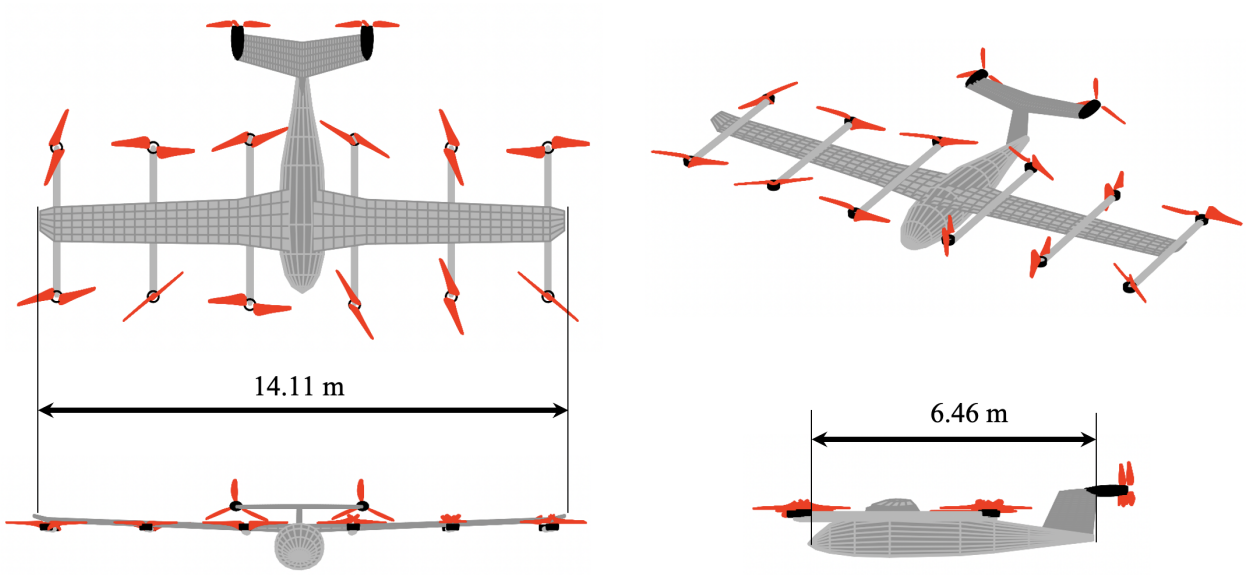

Flight Segment	Initial Altitude (ft)	Final Altitude (ft)	Initial Speed (mph)	Final Speed (mph)	Climb Rate (min)
VC	0	40	0	5.6	500
VT	40	40	5.6	101	0
CT	40	100	101	123	*
CL No.1	100	300	123	160	200
CL No.2	300	2500	160	175	500
CR	2500	2500	175	175	0
D No.1	2500	300	175	138	-300
RCL	300	1000	138	150	500
RCR	1000	1000	150	150	0
RD	1000	300	150	138	-300
D No.2	300	100	138	126	-300
AT	100	40	126	107	*
DT	40	40	107	3.4	0
VD	40	0	3.4	0	-300

C. Tandem Tilt-Wing eVTOL

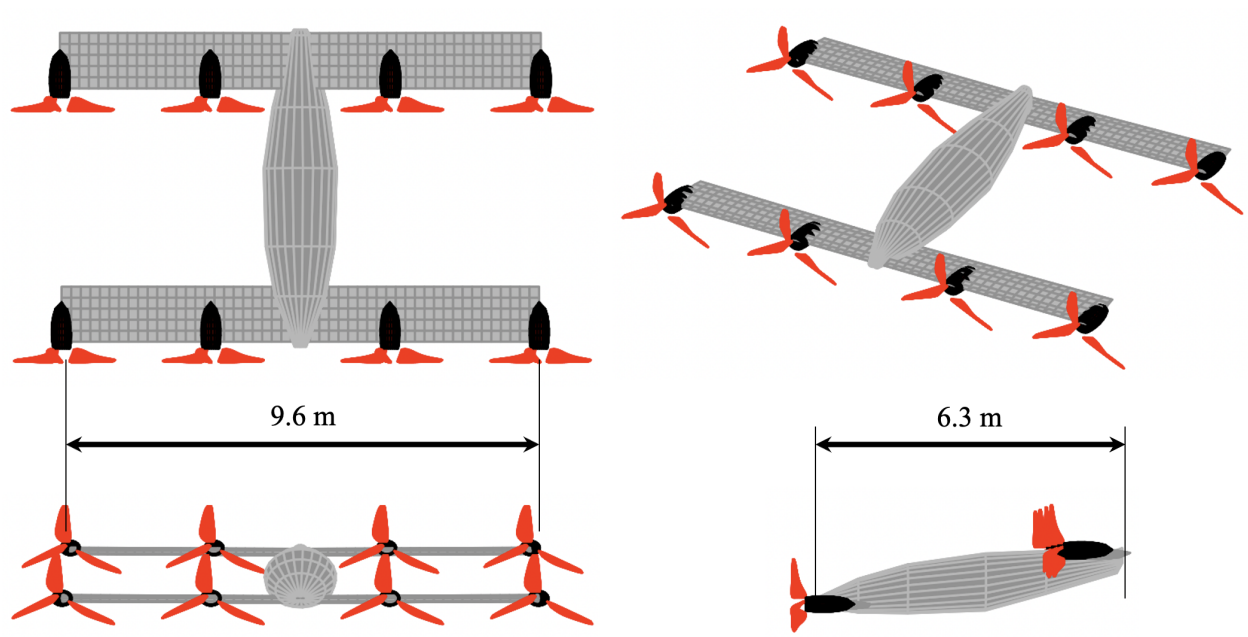

Flight Segment	Initial Altitude (ft)	Final Altitude (ft)	Initial Speed (mph)	Final Speed (mph)	Climb Rate (min)
VC	0	40	0	3.4	300
VT	40	40	3.4	55	0
CT No.1	40	100	55	85	500
CT No.2	100	100	85	125	0
CL	100	2500	125	175	500
CR	2500	2500	175	175	0
D	2500	100	175	125	-300
RCL	100	1000	125	150	500
RCR	1000	1000	150	150	0
RD	1000	100	150	125	-300
AT	100	40	125	55	-200
DT	40	40	55	3.4	*
VD	40	0	3.4	3.4	-300

D. Multi-Rotor eVTOL

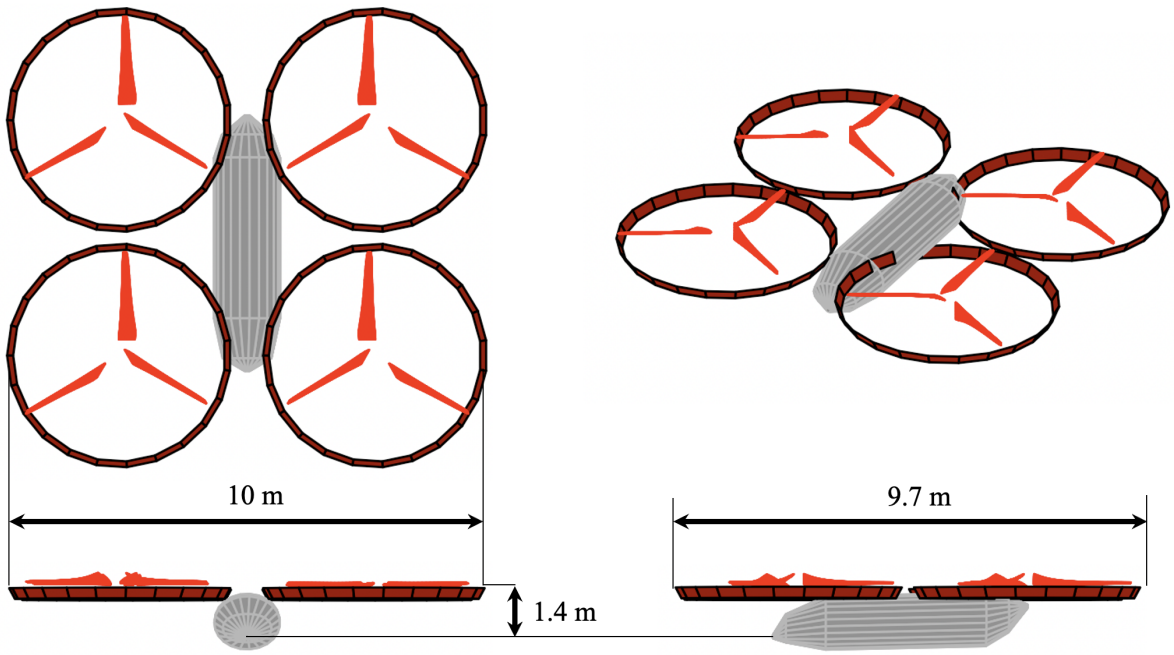

Flight Segment	Final Altitude (ft)	Initial Speed (mph)	Final Speed (mph)	Initial Speed (mph)	Climb Rate (min)
VC	0	40	0	3.4	300
VT	40	40	3.4	35	0
CL	40	2500	35	75	600
CR	2500	2500	75	75	0
D	2500	100	75	35	-200
RCL	100	1000	35	55	600
RCR	1000	1000	55	55	0
RD	1000	40	55	35	-200
DT	40	40	35	3.4	*
VD	40	0	3.4	0	-300

References

[1] Manyika J., et al., "Urban America: US Cities in the Global Economy," https://www.mckinsey.com/~/media/McKinsey/Featured%20Insights/Urbanization/US%20cities%20in%20the%20global%20economy/MGI_Urban_America_Full_Report.ashx, 2012.

[2] Ribeiro, S. K., Kobayashi, S., Beuthe, M., Gasca, J., Greene, D., Lee, D. S., Muromachi, Y., Newton, P. J., Plotkin, S., Sperling, D., et al., "Transportation and its infrastructure," 2007.

[3] Millard-Ball, A., "The autonomous vehicle parking problem," *Transport Policy*, Vol. 75, 2019, pp. 99 – 108. doi:https://doi.org/10.1016/j.tranpol.2019.01.003.

[4] AHS — The Vertical Flight Society, "Electric VTOL News," http://evtol.news/, 2018.

[5] Brown, A., and Harris, W., "A vehicle design and optimization model for on-demand aviation," *2018 AIAA/ASCE/AHS/ASC Structures, Structural Dynamics, and Materials Conference*, 2018, p. 0105.

[6] Duffy, M. J., Wakayama, S. R., and Hupp, R., "A Study in Reducing the Cost of Vertical Flight with Electric Propulsion," *17th AIAA Aviation Technology, Integration, and Operations Conference*, 2017, p. 3442.

[7] Warren, M. M., Garbo, A., Herniczek, M. T., Hamilton, T. K., and German, B. J., "Effects of range requirements and battery technology on electric vtol sizing and operational performance," *AIAA Scitech 2019 Forum*, , No. January, 2019, pp. 1–15. doi:10.2514/6.2019-0527.

[8] Bacchini, A., and Cestino, E., "Electric VTOL configurations comparison," *Aerospace*, Vol. 6, No. 3, 2019. doi:10.3390/aerospace6030026.

[9] Hepperle, M., "Electric Flight - Potential and Limitations," Tech. rep., Oct 2012.

[10] German, B., Daskilewicz, M., Hamilton, T. K., and Warren, M. M., "Cargo Delivery in by Passenger eVTOL Aircraft: A Case Study in the San Francisco Bay Area," *2018 AIAA Aerospace Sciences Meeting*, 2018. doi:10.2514/6.2018-2006.

[11] Duffy, M., Sevier, A. E., Hupp, R., Perdomo, E., and Wakayama, S., "Propulsion Scaling Methods in the Era of Electric Flight," *2018 AIAA/IEEE Electric Aircraft Technologies Symposium*, , No. July, 2018. doi:10.2514/6.2018-4978.

[12] "National Academies of Sciences, E., Medicine, and others", *Advancing aerial mobility: A national blueprint*, National Academies Press, 2020.

[13] Clarke, M., Botero, E., MacDonald, T., Erhard, R., Smart, J., and Alonso, J., "SUAVE 2.4.0," , May 2021. doi:10.5281/zenodo.4784705, URL https://doi.org/10.5281/zenodo.4784705.

[14] Uber, "Fast-Forwarding to a Future of On-Demand Urban Air Transportation," 2016.

[15] Lineberger, R., Hussain, A., Mehra, S., and Pankratz, D., "Elevating the Future of Mobility: Passenger drones and flying cars," https://www2.deloitte.com/content/dam/insights/us/articles/4339_Elevating-the-future-of-mobility/DI_Elevating-the-future-of-mobility.pdf, 2018.

[16] Bureau of Transportation Statistics, "U.S. On-Demand Air Taxi Safety Data," , Oct 2020. URL https://www.bts.gov/content/us-demand-air-taxia-safety-data.

[17] News", B., "Uber's self-driving operator charged over fatal crash," , Sep 2020. URL https://www.bbc.com/news/technology-54175359.

[18] Straubinger, A., Rothfeld, R., Shamiyeh, M., Büchter, K. D., Kaiser, J., and Plötner, K. O., "An overview of current research and developments in urban air mobility – Setting the scene for UAM introduction," *Journal of Air Transport Management*, Vol. 87, No. June, 2020. doi:10.1016/j.jairtraman.2020.101852.

[19] Moore, M. D., "Misconceptions of Electric Aircraft and their Emerging Aviation Markets," *52nd Aerospace Sciences Meeting*, 2014. doi:10.2514/6.2014-0535.

[20] Hwang, J. T., and Ning, A., "Large-scale multidisciplinary optimization of an electric aircraft for on-demand mobility," *2018 AIAA/ASCE/AHS/ASC Structures, Structural Dynamics, and Materials Conference*, 2018. doi:10.2514/6.2018-1384.

[21] Patterson, M. D., Antcliff, K. R., and Kohlman, L. W., "A proposed approach to studying urban air mobility missions including an initial exploration of mission requirements," *Annual Forum Proceedings - AHS International*, Vol. 2018-May, 2018.

[22] Federal Aviation Administration Advisory Council, "AC 150/5390-2: Heliport Design," https://www.faa.gov/documentLibrary/media/Advisory_Circular/150_5390_2c.pdf, Apr 2012.

[23] Katz, J., and Plotkin, A., *Low-Speed Aerodynamics*, Vol. 13, Cambridge University Press, 2001.

[24] Bertin, J. J., and Cummings, R. M., *Aerodynamics for Engineers Sixth Edition*, Vol. 6, Prentice Hall Upper Saddle River, NJ, 2015.

[25] Lukaczyk, T., Wendorff, A. D., Botero, E., MacDonald, T., Momose, T., Variyar, A., Vegh, J. M., Colonno, M., Economon, T. D., Alonso, J. J., Orra, T. H., and Ilario da Silva, C., "SUAVE: An Open-Source Environment for Multi-Fidelity Conceptual Vehicle Design," *AIAA Aviation*, Dallas, TX, 2015.

[26] Hubbard, H. H., "Aeroacoustics of Flight Vehicles: Theory and Practice Volume 1: Noise Sources," *NASA Reference Publication*, Vol. 1, No. 1258, 1991, p. 610. URL http://www.dtic.mil/dtic/tr/fulltext/u2/a241141.pdf#page=16.

[27] Hanson, D., "Sound from a propeller at angle of attack: a new theoretical viewpoint," *Proceedings of the Royal Society of London. Series A: Mathematical and Physical Sciences*, Vol. 449, No. 1936, 1995, pp. 315–328.

[28] Deming, A. F., "Noise from propellers with symmetrical sections at zero blade angle," 1937.

[29] Gutin, L., "On the sound field of a rotating propeller," 1948.

[30] Garrick, I., and Watkins, C. E., "A theoretical study of the effect of forward speed on the free-space sound-pressure field around propellers," 1953.

[31] Arnoldi, R. A., *Propeller noise caused by blade thickness*, United Aircraft Corporation, Research Department, 1956.

[32] Barry, F. W., and Magliozzi, B., "Noise detectability prediction method for low tip speed propellers," Tech. rep., United Technologies Corp Hamilton Standard Division, 1971.

[33] Smart, J., "Primary Weight Estimation for eVTOLs via Explicit Analysis and Surrogate Regression," *2019 AIAA Aviation Forum*, Dallas, TX, 2019.

[34] Adkins, C. N., and Liebeck, R. H., "Design of optimum propellers," *Journal of Propulsion and Power*, Vol. 10, No. 5, 1994, pp. 676–682. doi:10.2514/3.23779.

[35] Automotive & Industrial Systems Company of Panasonic Group, "Technical Information of NCR18650G," https://www.imrbatteries.com/content/panasonic_ncr18650g.pdf, . Accessed: 2020-01-30.

[36] Vegh, J. M., Botero, E., Clark, M., Smart, J., and Alonso, J. J., "Current capabilities and challenges of ndarc and suave for evtol aircraft design and analysis," *2019 AIAA/IEEE Electric Aircraft Technologies Symposium (EATS)*, IEEE, 2019, pp. 1–19.

[37] Wisk, "Meet Cora. Discover the future." , Jun 2020. URL https://wisk.aero/cora/.

[38] Acubed by Airbus, "Welcome to Vahana," , Sep 2016. URL https://acubed.airbus.com/blog/vahana/welcome-to-vahana/.

[39] Kim, S. H., Kim, Y. S., Baek, W. J., Heo, S., Yun, D. J., Han, S., and Jung, H., "Nanoscale Electrical Degradation of Silicon-Carbon Composite Anode Materials for Lithium-Ion Batteries," *ACS Applied Materials and Interfaces*, Vol. 10, No. 29, 2018, pp. 24549–24553. doi:10.1021/acsami.8b07012.

[40] Lu, L., Han, X., Li, J., Hua, J., and Ouyang, M., "A review on the key issues for lithium-ion battery management in electric vehicles," *Journal of Power Sources*, Vol. 226, 2013, pp. 272–288. doi:10.1016/j.jpowsour.2012.10.060.

[41] Reniers, J. M., Mulder, G., and Howey, D. A., "Review and Performance Comparison of Mechanical-Chemical Degradation Models for Lithium-Ion Batteries," *Journal of The Electrochemical Society*, Vol. 166, No. 14, 2019, pp. A3189–A3200. doi:10.1149/2.0281914jes.

[42] Howard, W. F., and Spotnitz, R. M., "Theoretical evaluation of high-energy lithium metal phosphate cathode materials in Li-ion batteries," *Journal of Power Sources*, Vol. 165, 2007, pp. 887–891. doi:10.1016/j.jpowsour.2006.12.046.

[43] Zhao, R., Zhang, S., Liu, J., and Gu, J., "A review of thermal performance improving methods of lithium ion battery: Electrode modification and thermal management system," *Journal of Power Sources*, Vol. 299, 2015, pp. 557–577. doi:10.1016/j.jpowsour.2015.09.001.